Novel Applications of Diffusion-Driven Flow

by

Michael R. Allshouse

B.S. Mechanical Engineering (2008)
Massachusetts Institute of Technology

Submitted to the Department of Mechanical Engineering
in partial fulfillment of the requirements for the degree of

Masters of Science in Mechanical Engineering

at the

MASSACHUSETTS INSTITUTE OF TECHNOLOGY

June 2010

Author .....
Department of Mechanical Engineering
May 17, 2010

Certified by .....
Thomas Peacock
Associate Professor
Thesis Supervisor

Accepted by .....
David Hardt
Chairman, Department Committee on Graduate Studies

Novel Applications of Diffusion-Driven Flow

by

Michael R. Allshouse

Submitted to the Department of Mechanical Engineering
on May 17, 2010, in partial fulfillment of the
requirements for the degree of
Masters of Science in Mechanical Engineering

Abstract

Diffusion-driven flow is the result of a conflict between hydrostatic equilibrium in a density stratified fluid and the no-flux boundary condition that must be obeyed on impermeable boundaries that are sloping with respect to gravity. This conflict results in a boundary layer flow, and in this thesis we present two novel applications of diffusion-driven flow. First, it is demonstrated that diffusion-driven flow can spontaneously propel asymmetric floating objects. Then, it is shown that the properties of diffusion-driven flow in a fissure can be exploited to make reliable measurements of molecular diffusivity.

Thesis Supervisor: Thomas Peacock
Title: Associate Professor

Acknowledgments

I would like to thank Professor Peacock for all his help throughout the entire research and writing processes. I truly appreciate the tremendous opportunity to work on a project with tons of potential. Also, his support and determined focus, helped us get through the rigors of experimental research, and his incredible patience helped make this thesis possible.

Thanks to Andy Gallant for all his work in designing and manufacturing the experimental apparatus. His assistance and advice in troubleshooting helped bring the experimental concepts to reality.

Additional thanks go to Michael Abruzzese and Kevin O'Keefe for making all the wedges used in the experiments and Bill Cormier for his help in constructing the thermal chamber and other various pieces of experimental equipment.

Thanks to Manikandan Mathur, Paula Echeverri, and Sasan Saidi for being soundboards for research, critiquing presentations, and making the lab a friendly and relaxed environment of study.

I could not have done this without my family and friends. Mom, your continuous encouragement and prayers have brought me through some of the tougher times. Dad, the eternal optimist, your faith in me has always pushed me forward. Sarah and Matt, without doubt, you two have always kept a smile on my face with your jokes and antics. Finally, thanks to all my friends particularly Ali, Dayan, Steven, John, and Nina for keeping me sane, letting me ramble about work, and making MIT feel like home.

Contents

List of Figures

Chapter 1

Introduction: Diffusion-Driven Flow

Diffusion-driven flow is a little-studied, spontaneous boundary layer flow that results from the combined influence of gravity and diffusion. This type of flow is prevalent throughout nature and is also closely related to the phenomena of glacier and valley winds [12][18]. Although diffusion-driven flow has historically been studied within the context of salt transport in rock fissures [17] and ocean boundary mixing [29], here we present two novel applications of the phenomenon that could have widespread potential impact. To provide the appropriate background, an overview of diffusion-driven flow is presented in this introduction, which includes some analysis, as a foundation for the work presented in later chapters, and a review of previous research. This chapter concludes with an outline of the remainder of the thesis.

1.1 Physical Explanation of Diffusion-Driven Flow

While investigating completely different physical problems, flows in a fissure and oceanic boundary mixing, respectively, Phillips [17] and Wunsch [29] independently and simultaneously discovered a new and fascinating form of boundary layer flow that spontaneously develops next to sloping boundaries in stratified fluids. This remarkable phenomenon is commonly referred to as *diffusion-driven flow*, and it arises

due to the interaction between hydrostatic equilibrium and impermeable boundary conditions.

A fluid system in hydrostatic equilibrium has constant density planes (isopycnals) aligned perpendicular to the direction of gravity. This can be understood using a simple oil and water arrangement [26]. In a system containing oil and water (two immiscible fluids), in which the direction of gravity points vertically down, a layer containing all of the (less-dense) oil will lie over a layer of the (more-dense) water. The same result of horizontal interfaces occurs in a three fluid system (e.g. oil-water-mercury), in which case a layer of lighter fluid (oil) will sit atop the medium-density fluid (water), which in turn overlies the densest fluid (mercury); the interfaces between each fluid layer are horizontal with respect to gravity. This scenario can be extended to systems with a continuous density stratification such as the ocean, where fluid density is continuously varying as a function of depth due to vertical variations in temperature and salt concentration. In hydrostatic equilibrium, all surfaces of constant density within the ocean are horizontal, oriented perpendicular with respect to gravity.

The other contributing factor to diffusion-driven flow is the impermeable (or no-flux) boundary condition which applies to the diffusion occurring in the system. Diffusion is the result of random particle motion, which over time redistributes particles and reduces concentration gradients [8]. Fick proposed a single law defining the process of diffusion and demonstrated that it satisfies the following relationship [9]:

$$\underline{J} = -\kappa \underline{\nabla} c, \tag{1.1}$$

where $\underline{J}$ is the diffusive flux vector that is anti-parallel to the concentration gradient, $\underline{\nabla} c$, and is scaled by the molecular diffusivity, κ. This relationship is used to derive the diffusion equation:

$$\frac{\partial c}{\partial t} + \underline{\nabla} \cdot (-\kappa \underline{\nabla} c) = 0. \tag{1.2}$$

An impermeable wall is defined as a boundary that does not allow a diffusive flux

through it, and by definition, this no-flux condition is modeled as

$$\underline{J} \cdot \hat{\underline{n}} = 0, \tag{1.3}$$

which in turn requires that

$$\hat{\underline{n}} \cdot (\underline{\nabla} c) = 0 \tag{1.4}$$

along the impermeable wall, where $\hat{\underline{n}}$ is the unit vector normal to the wall. Based on this condition, isopycnals must always be perpendicular to an impermeable boundary to ensure that there is no gradient in density normal to the wall, and thus no diffusive flux normal to the boundary.

The work of Phillips [17] and Wunsch [29] reveals that a conflict arises between the requirements of hydrostatic equilibrium and a no-flux condition along a sloping boundary. At vertical walls, horizontal isopycnals can remain horizontal, but in systems with sloping sidewalls (Figure 1-1) the no-flux boundary condition requires isopycnals to bend away from horizontal to be normal to the wall. This bending is inconsistent with hydrostatic equilibrium, as fluid adjacent to the sloping boundary differs in density compared to fluid at the same vertical level away from the wall. The fluid adjacent to the wall therefore experiences a buoyancy force that produces a flow upwards along the underlying wall. Similarly, if a sloping wall bounds the fluid from above, a downward boundary flow will develop.

1.2 Analysis of Diffusion-Driven Flow

In his pioneering study, Phillips [17] develops a two-dimensional analytical model for diffusion-driven flow along a sloping wall in a semi-infinite fluid, which is the scenario presented in Figure 1-1. This analysis assumes a steady-state solution for which all velocity variations are only a function of the wall normal-coordinate η. Due to the along-wall velocity being independent of the along-wall coordinate, it is necessary to assume that the solution is unidirectional (i.e. no flow normal to the wall in the

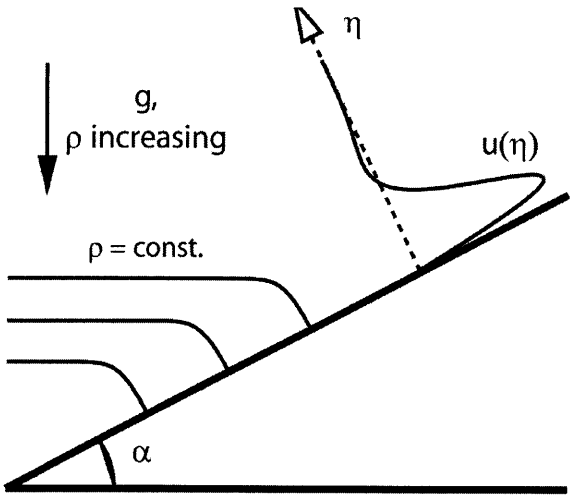

Figure 1-1: A sketch of the constant density lines in a stratified system along a sloping boundary resulting in diffusion-driven flow up the wall. A sample velocity profile is shown at the top right as a function of the distance normal to the wall, η.

boundary layer) in order to satisfy the continuity equation:

$$\underline{\nabla} \cdot \underline{q} = 0 \tag{1.5}$$

where $\underline{q}$ is the velocity vector.

The other governing equations are the Navier-Stokes equations in two-dimensions,

$$\rho \frac{\partial \underline{q}}{\partial t} + \rho(\underline{q} \cdot \underline{\nabla})\underline{q} = -\underline{\nabla} p + \mu \nabla^2 \underline{q} + \rho \underline{g}, \tag{1.6}$$

and the diffusion equation,

$$\frac{\partial \rho}{\partial t} + \underline{\nabla} \cdot (-\kappa \underline{\nabla} \rho) = -(\underline{q} \cdot \underline{\nabla})\rho, \tag{1.7}$$

where ρ is the density, μ the dynamic viscosity of the fluid, p the pressure, and $\underline{g}$ is the gravity vector. If a steady-state, unidirectional flow is assumed, Equations (1.6) and (1.7) reduce to:

$$-\frac{\partial p}{\partial \eta} - \rho g \cos\alpha \;\; = \;\; 0, \tag{1.8}$$

$$-\frac{\partial p}{\partial \zeta} + \mu \frac{\partial^2 u}{\partial \eta^2} - \rho g \sin\alpha = 0, \tag{1.9}$$

$$u\frac{\partial \rho}{\partial \zeta} = \kappa\left(\frac{\partial^2 \rho}{\partial \zeta^2} + \frac{\partial^2 \rho}{\partial \eta^2}\right), \tag{1.10}$$

where ζ is the along wall coordinate and α is the slope angle.

In order to solve the above set of equations, boundary conditions must be applied. At the sloping wall, the no-slip condition requires

$$u(\eta) = 0 \text{ at } \eta = 0, \tag{1.11}$$

and since the wall is impermeable,

$$\frac{\partial \rho}{\partial \eta} = 0 \text{ at } \eta = 0. \tag{1.12}$$

Infinitely far from the wall, it is assumed that the boundary layer perturbation near the wall does not impact either the bulk density or velocity profiles. Thus

$$u(\eta) \to 0 \text{ as } \eta \to \infty \tag{1.13}$$

and

$$\rho \to \rho_o + \frac{d\rho}{dz}(\zeta \sin\alpha + \eta \cos\alpha) \text{ as } \eta \to \infty, \tag{1.14}$$

where ρ_o is the density at the origin of the coordinate system on the wall and z is the vertical coordinate anti-parallel to gravity.

With the no-slip (eq. 1.11) and no-flux conditions (eq. 1.12) at the wall, as well as the matching condition (eqs. 1.13 and 1.14) infinitely far from the wall, it is possible to show that the momentum equations (eqs. 1.8 and 1.9) and the diffusion equation (eq. 1.10) can be solved explicitly for the three variables ($p, \rho,$ and u). The resulting velocity profile is

$$u(\eta) = 2\kappa\gamma \cot\alpha e^{-\gamma\eta} \sin(\gamma\eta) \tag{1.15}$$

where

$$\gamma = \left(\frac{N^2 \sin^2 \alpha}{4\nu\kappa} \right)^{1/4} \tag{1.16}$$

is the inverse length scale of the boundary layer thickness, which is a function of the buoyancy frequency,

$$N = \sqrt{-\frac{g}{\rho_0} \frac{\partial \rho}{\partial z}}. \tag{1.17}$$

From this result, a characteristic velocity of diffusion-driven flow is

$$u_{pw} = 2\kappa\gamma \cot\alpha. \tag{1.18}$$

Given the velocity profile (eq. 1.15), it is possible to calculate the volume flux, Q, along a sloping wall. The result,

$$Q = \int_0^\infty u d\eta = \kappa \cot\alpha, \tag{1.19}$$

yields the interesting result that the volume flux is simply a function of the diffusion coefficient and the slope angle, and is independent of the local fluid density, density gradient and viscosity.

1.3 Previous Studies of Diffusion-Driven Flow

Despite the simplicity of the arrangement needed to produce diffusion-driven flow, which make it a rule rather than exception in fluid systems with a density stratification, there have been relatively few studies of this phenomenon. This thesis presents the results of investigations of two original ideas that build upon the small body of research that exists for diffusion-driven flow. Here, a summary of the previous work is provided.

Boundary-driven mixing was the focus of the study by Woods [27], who investigate the impact that diffusion-driven flow at sloping side walls has on the interior stratification in a closed container. The principal reason for the impact of diffusion-driven flow is that in a closed container the flow along the sloping boundaries must

be balanced by a return flow in the bulk, which in turn affects the stratification. A modified diffusion equation that is based upon vertical variations of horizontal cross-section is derived, which predicts significant impact on the interior stratification only if the boundary-layer flows are turbulent. An interesting idea that arises from this work is that diffusion-driven flows can have a significant impact in dense granular beds.

In an analytic study of diffusion-driven flow, Woods and Linz [28] investigate the flow that develops in tilted rock fractures due to temperature influencing the density. They show that a flow is always produced for a tilted fracture and proceed to derive a dispersion relation for passive particles which diffuse in the fluid. Because of the flow that develops, the dispersion rate can be two to three orders of magnitude larger than the molecular diffusion rate. A similar process will occur if there is a salt stratification, but if thermal and salt stratifications exist, double diffusion can either help or hinder the dispersion rate.

Luna *et al.* [11] analyzed the diffusion-driven flow in a rock fissure discussed by Woods and Linz [28] and tested it experimentally. They started by presenting a detailed study of the temperature distribution in the walls provided the top and bottom of the system are held at constant temperature. The temperature variation causes convection in the tilted fissure which is then studied. Using Particle Imaging Velocimetry (PIV), they measure the induced velocity field and demonstrate that it matches the theoretical predictions of Woods and Linz [28].

An experimental parameter study of diffusion driven flow is performed by Peacock, Stocker, and Aristoff [16] and Heitz, Peacock, and Stocker [10]. The first study analyzes the dependence of diffusion-driven flow speed on angle of inclination for an arrangement that approximates a semi-infinite system [16]. With a tank containing a stratified fluid and a sloping boundary, diffusion-driven flow is induced and carries a dye up the wall while the system is imaged. The dye has a slow diffusion rate in comparison to the speed of the fluid, so all dye movement is credited to fluid convection. The flow speeds observed over large angles agree with Phillips theoretical predictions [17], but for angles smaller than a critical value (5^o) the experimental

results depart from the theoretical prediction. Further research in the optimization of the flows in a fissure is presented by Heitz, Peacock, and Stocker [10]. In this experimental study, they conclude that by changing the gap thickness and angle it is possible to maximize the transport speed of diffusion-driven flow in a tilted channel.

A numerical and analytic study of the flow that develops around a suspended sphere in a stratified fluid is presented by Baidulov *et al.* [2]. They discover that horizontal flow layers develop near the sphere's poles and convection cells cycle fluid in the vicinity of the sphere. A schlieren visualization is also performed and demonstrate the layering that occurs near the top and bottom of the sphere.

Page and Johnson [14] extend the analysis of Phillips [17] by analyzing diffusion-driven flow in a finite domain. In their analysis, they account for the fact that sudden changes in slope of a boundary (e.g. at a corner) require entrainment and expulsion of fluid from the boundary. Their initial work is a linear analysis of this effect [14], but they further developed their theory to incorporate non-linear effects, which results in their theoretical model agreeing with numerical simulations [15].

1.4 Overview of Thesis

With a basic overview of diffusion-driven flow having been presented, the work presented in subsequent chapters addresses two novel applications of diffusion-driven flow. The first set of investigations, presented in Chapter 2, demonstrates that diffusion-driven flow can propel an asymmetric object horizontally through a stratified fluid. Thereafter, in Chapter 3, it is demonstrated that diffusion-driven flow provides an accurate and reliable means of making measurements of molecular diffusivity. Concluding remarks, as well as, a discussion of future research directions, are presented in Chapter 4.

Chapter 2

Propulsion through Diffusion-Driven Flow

A new method of propulsion in stratified fluid systems is proposed, demonstrated, and investigated in this chapter. Specifically, we find that the conversion of disordered microscopic energy to motion of a macroscale floating object is possible by exploiting diffusion-driven flow. We first presents the fundamental reasoning of how propulsion occurs. Experimental results are then presented demonstrating the propulsion of an object and the influence of various physical parameters on the motion. After the parameter studies, flow visualization experiments are performed. These results are then compared with a three-dimensional numerical simulation, which provides significant insight into the propulsion mechanism. Finally, concluding remarks are presented, as well as suggestions for applications and future research.

2.1 Physical Basis for Diffusion-Driven Propulsion

As described in Chapter 1, diffusion-driven flow occurs along all sloping boundaries of a stratified system. Notably, Baidulov *et al.* [2] study the induced diffusion-driven flow around a submerged sphere and, through schlieren visualization, demonstrate that diffusion-driven flow forms symmetrically around the sphere. In these experiments, the sphere is fixed by virtue of being suspended from a wire. The idea pursued

in this chapter, however, is whether an object that is freely floating and generating diffusion-driven flows over its sloping surfaces might actually be propelled as a result of these flows.

Based on the results of Baidulov *et al.* [2], an axi-symmetric flow structure develops around a sphere, and thus any resultant surface forces, must be balanced (e.g. pressure perturbations on one side of the sphere are equally matched by pressure perturbations on the opposite side). It is therefore expected that a freely floating sphere will remain stationary at its height of neutral buoyancy, with zero net force arising from diffusion-driven flow. If, however, an asymmetric object is floating in a stratified fluid, it seems plausible to expect motion to result from the diffusion-driven flows over its surface, since the symmetric force balance achieved around a sphere no longer exists, and there is the potential for a net force to arise on the object. As a simple example of an asymmetric object, we consider an isosceles triangular prism, or wedge, as shown in Figure 2-1. For the orientation shown, diffusion-driven flow must occur along the two sloping sides and it is hypothesized that this will create an asymmetric flow structure, resulting in motion of the wedge.

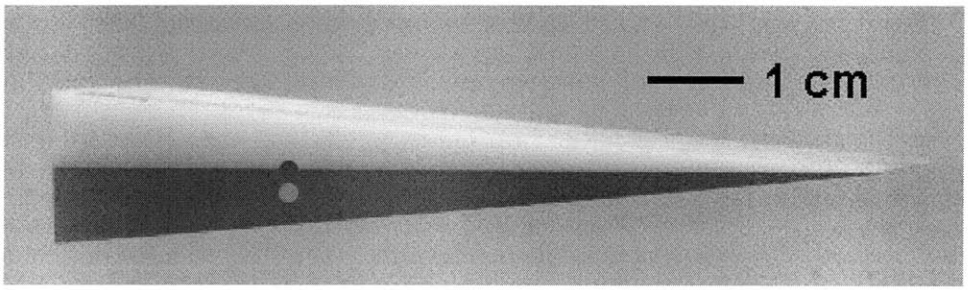

Figure 2-1: A triangular wedge floating in a stratification. The red dot represents the center of buoyancy and the green dot is the center of mass.

2.2 Experimental Procedure

To test the hypothesis of propulsion of an asymmetric object via diffusion-driven flow, an experiment is designed and executed using the triangular wedge presented in Figure 2-1. The experimental procedure includes establishing a density stratification,

using a cage mechanism to release the wedge in quiescent fluid, and devising a means of visualizing the motion of the wedge. Finally, in order to analyze the results of an experiment, a motion-tracking algorithm is developed.

2.2.1 Wedge Design

The main features of the wedge that must be accounted for in its design are that it should float in water and be stable in the orientation shown in Figure 2-1. In order for the wedge to float in a salt-water system, the average density of the wedge must lie in the range of densities of salt water ($1000 - 1200$ kg/m^3). Ideally, the density of the wedge is around 1100kg/m^3, which allows flexibility in setting the salt-water stratification parameters. To ensure the wedge stably floats with a horizontal orientation, the center of mass must lie below the center of buoyancy in this orientation, as illustrated in Figure 2-1. If this is achieved, any perturbation from the desired orientation produces a restoring torque about the center of buoyancy.

To satisfy the aforementioned requirements, the wedge used in the experiments is comprised of two different plastics: high-density Polyethylene (the white, top half of the wedge, $\rho = 955$ kg/m^3) and Ultem (the brown, bottom half of the wedge, $\rho =$ 1280kg/m^3). Using these plastics, the net density of the total wedge is approximately 1118kg/m^3, neglecting the weight of the epoxy holding the halves together, and the center of mass is located approximately 0.5mm below the center of buoyancy, which essentially lies on the centerline.

Although, in principle, the wedge design is such that it should float horizontally, in practice, imperfections in machining and the use of glue to join the two pieces of plastic mean that initially a wedge is not perfectly balanced. To level it, images are taken to determine any tilt in the wedge compared with a vertical plumb line. Then, sand paper is used to modify the wedge in such a way that it floats level to within $\pm 0.1^o$.

Once the wedge is level, it is still possible for it to become imbalanced if an air bubble forms on its surface; the resulting buoyancy force from the bubble will change the orientation of the wedge. Two precautions are taken to prevent this scenario.

First, the water used in the experiments is left to sit overnight to degas. Second, a polyurethane coating is applied to the surface of the wedge to suppress the formation of bubbles by virtue of smoothing the surface and thereby reducing the possibility of nucleation sites for bubble formation.

2.2.2 Experimental Procedure

A schematic of the experimental arrangement is presented in Figure 2-2. The tank used for almost all experiments is a 30cm-wide × 40cm-long × 40cm-tall acrylic tank. A larger tank measuring 55cm-wide × 75cm-long × 40cm-tall is also utilized. False vertical walls can be inserted into the tanks, allowing the flexibility to create a range of domain sizes, which in turn enables systematic investigation of the effect of the tank size on the wedge speed. One negative aspect of using a larger tank, however, is that viscous damping takes longer to suppress disturbances due to random thermal fluctuations, and so thermal convection develops more readily as the Rayleigh number goes up proportional to the volume.

Two types of fluids are used for the experiments. For a majority of the experiments the working fluid used is tap-water. For a few experiments, however, a water-glycerol mix is used. To stratify these fluids, the solutes used in the experiments are: sodium chloride (NaCl), potassium chloride (KCl), and magnesium chloride ($MgCl_2$). Since the average density of the wedge is 1118kg/m^3, the density stratification is chosen so that this is the density of the working fluid at the mid-depth of the experimental tank. All experiments feature a linear stratification which is established by the Oster double bucket method [13]. The pump used for this process is a Masterflex I/P peristaltic pump. To confirm the filling successfully creates a linear stratification, fluid samples are withdrawn using a needle and syringe and the sample densities are measured. Finally, a saran wrap cover is placed on the top of the tank to prevent convection and evaporation of the fluid.

With the tank filled, the wedge is submerged in the system. A cage consisting of vertical bars is lowered into the fluid via a linear traverse, and the wedge, floating at its neutral buoyancy height, is confined between the vertical bars so that it cannot

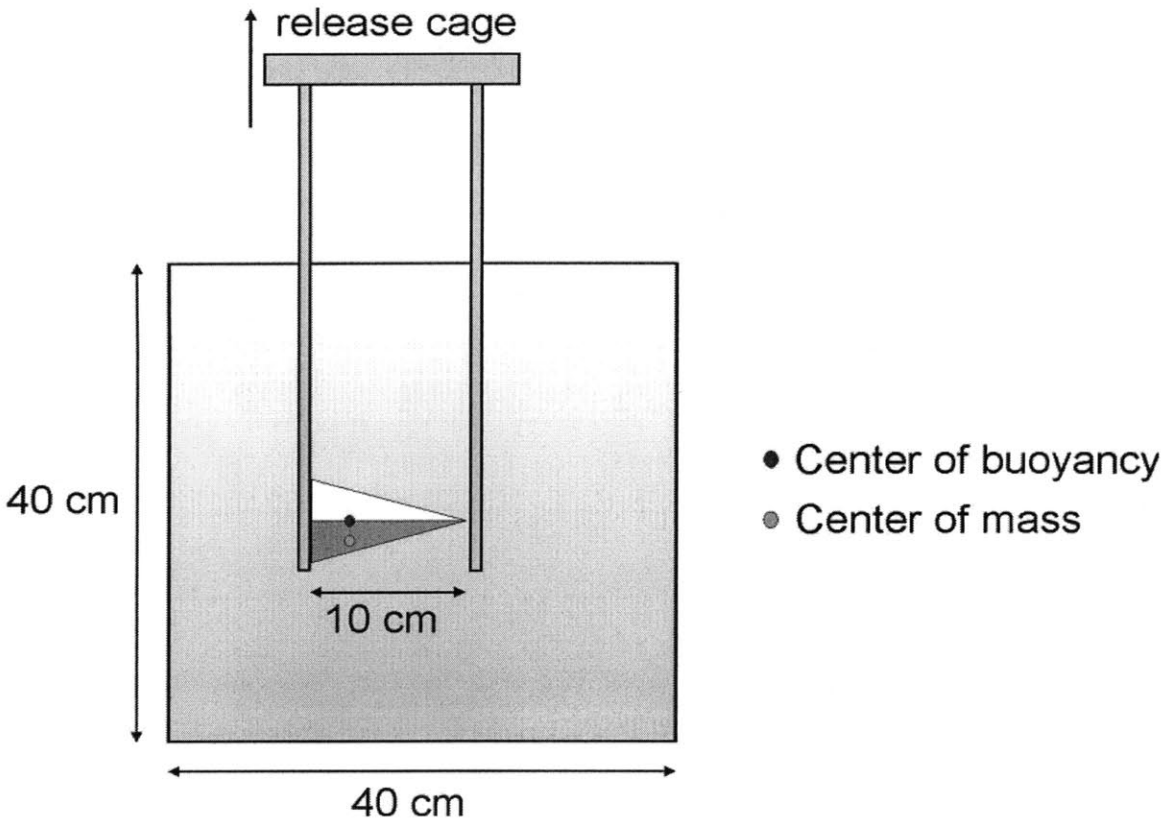

Figure 2-2: A sketch of the experimental system used. The neutrally buoyant wedge floating in a stratified fluid is contained within a vertical bar cage.

move in the horizontal plane. After capture of the wedge within the cage, the entire system is left to stand for an hour or longer to establish a quiescent state. Thereafter, the wedge is released by slowly raising the vertical bars out of the system at a rate of $\sim 2 \times 10^{-4}$m/s.

A Cannon EOS 30D camera, operated in time-lapse mode using computer control, is used to record images of the motion of the wedge every ten minutes. The camera is either mounted above or to the side of the system, depending on which perspective needs to be captured. For most experiments, the pictures are taken from above, which allows tracking of the position of the wedge in the horizontal plane as a function of time. The location is tracked by placing red markers on the wedge in each image using Microsoft Paint; a sample image is shown in Figure 2-3. A Matlab script is then used to track the location of the dots, and the distance traveled by the wedge is determined by scaling the marker displacement with the wedge dimensions. Given

the marker displacement as a function of time, the velocity and orientation of the wedge can be determined. If the wedge does not travel in a straight line at constant velocity, the experiment is rerun because this means that either the wedge is not balanced or there is convection driven by an external source (e.g. thermal gradients).

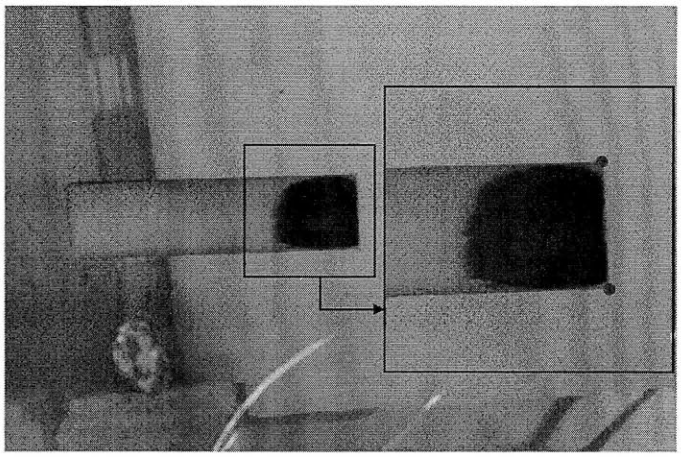

Figure 2-3: Image of the wedge taken from above. Inset shows the locating dots added at the corners of the wedge.

2.3 Demonstration of Propulsion through Diffusion

To demonstrate propulsion due to diffusion-driven flow, the first experiment performed involves a sphere submerged in a stratified fluid. The NaCl stratified system has a gravitationally stable density gradient $d\rho/dz = -511 \pm 3\text{kg/m}^4$. The sphere used is a 19.05mm-diameter polyurethane sphere of density $\rho = 1115\text{kg/m}^3$ coated with a polyurethane spray to prevent air bubbles forming on its surface. The results from this experiment are shown in Figure 2-4a. Clearly there is no motion of the sphere, which indicates that neither diffusion-driven flow, nor ambient currents, drive the sphere to move.

After completing the sphere test, a wedge measuring 10cm-long, 2.5cm-wide, and 5^o slope angle is submerged in the same stratified system and released using the cage mechanism. Time stamped images of the wedge are presented in Figure 2-4b, in which

it is clear that the wedge is propelled in the direction of its tip. The wedges position as a function of time is shown in Figure 2-4c, from which a constant velocity of 10.2×10^{-3} m/h can be calculated. This result is repeatable and demonstrates that, in contrast to symmetric objects such as a sphere, an asymmetric object spontaneously moves horizontally in a stably-stratified system, the likely cause being diffusion-driven flow.

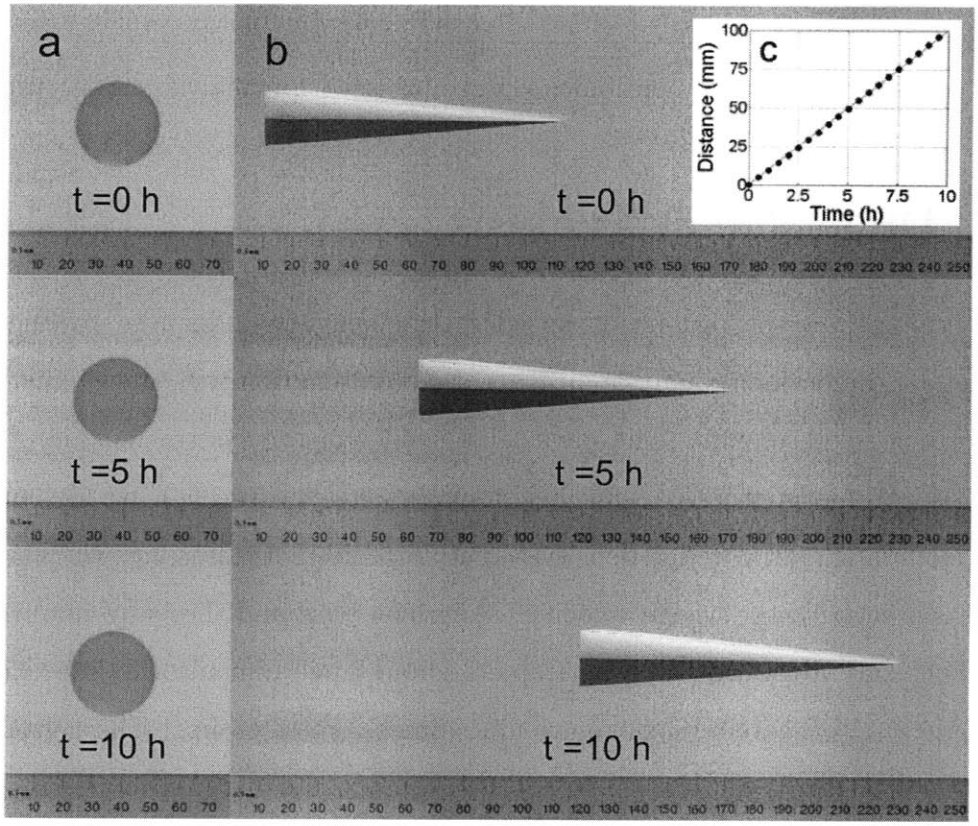

Figure 2-4: (a) A polyurethane sphere floating in a stratification of strength $d\rho/dz = -511 \pm 3\text{kg/m}^4$. The images taken at five hour intervals showing no motion. (b) A plastic wedge floating in the same stratification. The time-lapse images reveal forward motion. (c) Wedge position vs. time plot.

It now remains to determine how the system parameters, such as the strength of stratification and the size of the wedge, influence the propulsion speed. Furthermore, it is important to discover the nature of the flow fields in the vicinity of the wedge due to diffusion-driven flow and to better understand the nature of the propulsive force.

Π group	Parameter Function	Description
Π_1	u/u_{pw}	Velocity ratio
Π_2	L/l	Length ratio
Π_3	W/w	Width ratio
Π_4	$H/l\alpha$	Height ratio
Π_5	$u_{pw}w/\nu$	Reynolds number
Π_6	u_{pw}/Nl	Froude number
Π_7	κ/ν	Schmidt number
Π_8	w/l	Wedge aspect ratio
Π_9	α	Wedge Inclination Angle

Table 2.1: Table of the dimensionless Π groups used for analysis of the propulsion speed.

2.4 Dimensional Analysis

To determine how the propulsion speed of the wedge is influenced by the system parameters, dimensional analysis [6] is used in combination with a systematic series of laboratory experiments. The physical variables of the system include: the tank width (W), tank length (L), tank height (H), wedge width (w), wedge length (l), wedge slope angle (α), wedge density (ρ), fluid molecular diffusivity (κ), fluid kinematic viscosity (ν), the wedge velocity (u), gravity (g), and the buoyancy frequency (N). There are a total of twelve parameters and three dimensions, so according to Buckinghams Pi theorem [6] there are nine dimensionless groups. These groups may be chosen arbitrarily, but a sensible choice of groups is listed in Table 2.1.

The objective of this study is to understand how the dimensionless speed, Π_1, is a function of the other Pi groups. The Pi groups can be organized into three categories. The first category is concerned with the influence of confinement on the propulsion speed, and contains the groups Π_2, Π_3, and Π_4 that relate the size of the wedge to the size of the experimental tank. The second category contains groups that concern physical properties of the fluid flows. This includes the Reynolds number, Π_5, which is a ratio of inertial to viscous forces, the Froude number, Π_6, which is the ratio of inertial to buoyancy forces, and the Schmidt number, Π_7, which is the ratio of molecular and viscous diffusivity. The third, and final, category involves the groups Π_8 and Π_9 that define the shape of the wedge.

To summarize, we now proceed, via a series of experiments, to study the functional relationship

$$\frac{u}{u_{pw}} = f\left(\frac{L}{l}, \frac{W}{w}, \frac{H}{l\alpha}, \frac{u_{pw}w}{\nu}, \frac{u_{pw}}{Nl}, \frac{\kappa}{\nu}, \frac{w}{l}, \alpha\right). \tag{2.1}$$

2.4.1 Confinement Studies

The first goal of the experiments is to determine if it is possible for the wedge to act as if it is unconfined. If so, the dimensionless speed must be independent of the groups Π_2, Π_3, and Π_4. A number of experiments are performed in which the fluid and wedge parameters remain constant while the size of the tank is changed through the use of false walls. For all these experiments, NaCl is used to stratify the water and the wedge is 10cm long and 2.5cm wide, with a 5^o slope.

The first series of experiments demonstrates the influence of the ratio of the tank length to the wedge length. These experiments are run using a density gradient of $d\rho/dz = -430\text{kg/m}^4$. Six different length ratios are tested, ranging from $L/l = 1.5$ to $L/l = 5$, and the results, presented in Figure 2-5, reveals that the length ratio plays essentially no role in setting the propulsion speed. There is a deviation of less than three percent in the non-dimensional speed for the length ratios above two, and this variation is likely due to slight changes in stratification due to the removal and replacement of the false wall.

The next series of experiments studies the impact of the width ratio on the velocity. In this case, the experiments are run for two different stratifications: $d\rho/dz = -525\text{kg/m}^4$ and $d\rho/dz = -50\text{kg/m}^4$, and the results are presented in Figure 2-5. The non-dimensional speed decreases with the width ratio for $W/w < 5$ for both stratification strengths. The reason for running the second stratification is to confirm that the influence on the non-dimensional speed is not a function of the stratification. Based on these results, it can be concluded that the propulsion speed is independent of the width ration for $W/w > 6$.

While no systematic tests are run to determine if the height of the system modifies the non-dimensional velocity, the flow visualization experiments described later reveal no induced flow significantly above or below the wedge. Furthermore, to achieve

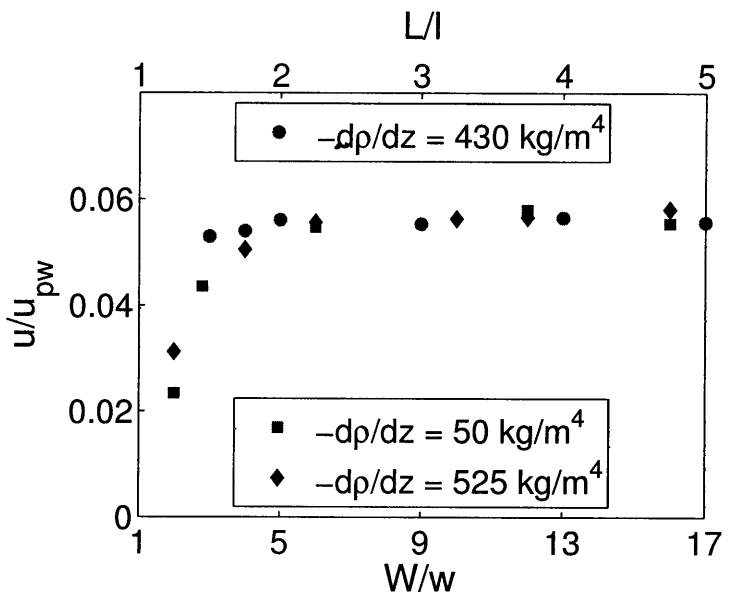

Figure 2-5: Plot showing the relationship between the non-dimensional velocity, u/u_{pw}, and the length ratio, L/l, and width ratio, W/w. The length ratio results are for $d\rho/dz = -430\text{kg/m}^4$, shown as red dots. The width ratio tests are for $d\rho/dz = -50\text{kg/m}^4$ (blue squares) and $d\rho/dz = -525\text{kg/m}^4$ (black diamonds).

very strong stratification, the water depth is changed throughout several of the other experiments without changing the non-dimensional speed. Thus it is reasonably concluded that provided the wedge is floating freely in the tank, the height ratio does not impact the propulsion speed.

Given a non-dimensional speed is asymptotically approached as both length and width ratios increase, the unconfined non-dimensional velocity is obtained provided $L/l > 2$ and $W/w > 6$. For the remainder of the parameter studies, the experiments are performed in this regime and we proceed to determine the functional relationship

$$\frac{u}{u_{pw}} = f\left(\frac{u_{pw}w}{\nu}, \frac{u_{pw}}{Nl}, \frac{\kappa}{\nu}, \alpha, \frac{w}{l}\right). \tag{2.2}$$

2.4.2 Fluid Parameter Studies

2.4.2.1 Froude and Reynolds Numbers Experiments

It is next determined how the Reynolds and Froude numbers influence the non-dimensional speed of the wedge. In so doing, it is important to note that both the Reynolds and Froude numbers are directly proportional to the characteristic velocity of diffusion-driven flow, u_{pw}. Since this characteristic velocity is a function of the stratification, as characterized by the buoyancy frequency, N, both the Reynolds and Froude numbers vary with the stratification strength. The typical values of the Reynolds and Froude number are $0.1 - 1.5$ and $1.0 \times 10^{-4} - 5.0 \times 10^{-4}$.

The stratification, as well as the stratifying agent, are changed in these studies while all other parameters are held constant. More specifically, a series of experiments varying the stratification are run for each of the three stratifying agents: NaCl, KCl, and $MgCl_2$. The stratification ranges for each of these agents are: 20-500kg/m^4 for NaCl, 40-800kg/m^4 for KCl, and 40-900kg/m^4 for $MgCl_2$. The parameters that are held constant are the tank size (30cm width, 40cm length) and the wedge shape ($\alpha = 5^o$, $l = 10$cm, $w = 2.5$cm). For lower stratification strengths, there is a higher susceptibility to disturbances due to weaker viscous damping and higher convection compared to stronger stratified systems. To compensate for these disturbances, some experiments are run multiple times at the weakest stratifications.

The results of these studies are presented in Figure 2-6, in which it can be seen that the velocity increases by almost an order of magnitude over the range of stratifications tested. The highest velocities are for potassium chloride, which has the highest molecular diffusivity, while magnesium chloride, which has the lowest molecular diffusivity, has the lowest velocities. For all three stratifying agents, on this log-log plot a line of slope 0.25 ± 0.02 is found to give a best fit to the data. Thus it is revealed that

$$u \propto \frac{d\rho}{dz}^{1/4} \Rightarrow u \propto u_{pw} \tag{2.3}$$

independent of stratifying agent.

With the conclusion that the non-dimensional speed does not change with the

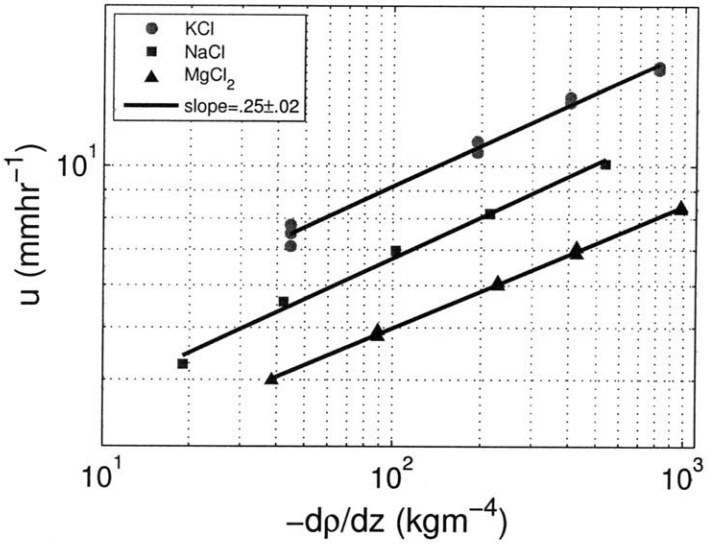

Figure 2-6: Log-log plot showing the relationship between the dimensional velocity, u, and the stratification strength, $d\rho/dz$. Experiments are run using NaCl, KCl, and $MgCl_2$. Lines of slope 0.25 are shown fitting the data.

stratification, the influence of the Reynolds and Froude numbers can be resolved. Since both of these dimensionless numbers are functions of the characteristic speed, it can be concluded that changing the Reynolds and Froude number does not change the non-dimensional speed. Thus, we now seek to investigate the functional relationship

$$\frac{u}{u_{pw}} = f\left(\frac{\kappa}{\nu}, \frac{w}{l}, \alpha\right). \tag{2.4}$$

2.4.2.2 Schmidt Number Experiments

The next series of experiments investigate the influence the Schmidt number, Sc, has on the non-dimensional velocity of the wedge. For each combination of solvents and solutes, a different kinematic viscosity and diffusion coefficient are measured to determine Sc. The wedge and tank sizes used in this study are the same as in the previous section.

To vary the Schmidt number the following salts are used in tap-water: NaCl, KCl, and $MgCl_2$. The previous section presents results in which these salts are used as stratifying agents to analyze the relationship between the stratification strength

Solvent	Solute	Viscosity (m^2/s)	Diffusivity (m^2/s)
KCl	Tap Water	1.62e-9	0.854e-6
NaCl	Tap Water	1.35e-9	1.09e-6
$MgCl_2$	Tap Water	0.96e-9	1.53e-6
NaCl	Tap Water / Glycerol (3142)	1.07e-9;	1.52e-6
NaCl	Tap Water / Glycerol (2134)	0.90e-9;	1.92e-6
NaCl	Tap Water / Glycerol (1424)	0.75e-9;	2.36e-6

Table 2.2: Table of measured viscosities and diffusivities for the salt/solvent mixes used for the Schmidt number experiments.

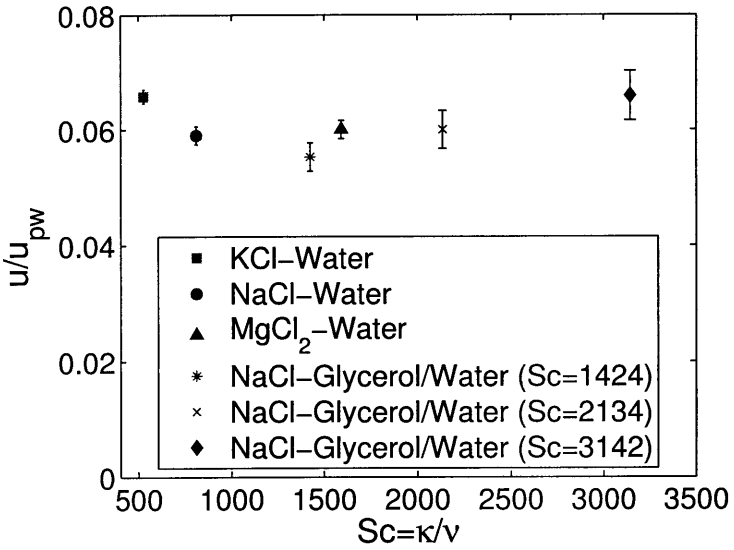

Figure 2-7: Plot showing the relationship between the non-dimensional velocity, u/u_{pw}, and the Schmidt Number, κ/ν.

and the velocity. These results collapse to give a non-dimensional speed for each of the three different Schmidt numbers. In addition to these results, three water/glycerol mixtures are created and stratified using NaCl. Each of these fluid systems also has a unique Sc and resulting wedge velocity. The kinematic viscosity and molecular diffusivities for all the experiments are presented in Table 2.2.

The results of the six different experiments are presented in Figure 2-7. With the glycerol/water mixtures fewer tests are run, which results in a larger uncertainty in the exact value of the non-dimensional velocity. All the non-dimensional velocities fall into the range of .055 to .065, however, and to within experimental error there is no obvious trend, leading us to conclude that the influence of the Schmidt number

is very weak and can be neglected. Thus, the dimensionless propulsion speed is only a function of the wedge geometry and it remains only to investigate the functional relationship

$$\frac{u}{u_{pw}} = f\left(\frac{w}{l}, \alpha\right). \tag{2.5}$$

2.4.3 Wedge Geometry Studies

2.4.3.1 Influence of Slope Angle

The next series of tests determines the influence of the wedge slope angle on the propulsion speed. Equation (1.18) presents the inverse dependence of the diffusion-driven velocity speed on the slope angle, revealing that as the angle increases the characteristic velocity decreases. If we find that the non-dimensional speed does not change as a function of angle, this indicates that all angular dependence is determined by the characteristic velocity.

To test influence of the slope angle, we use a NaCl stratification of strength $d\rho/dz = -500\text{kg/m}^4$ inside the 30 $\times$ 40cm tank. Several new 10cm long $\times$ 2.5cm wide wedges are manufactured with slope angles $2.5^o, 5^o, 7.5^o, 15^o$, and 30^o. Wedges of smaller angle could not be made due to the difficulty of manufacturing a wedge so thin, and wedges of larger angle would not move fast enough for us to easily detect the motion. With the manufactured wedges, experiments for each wedge are repeated several times to ensure a good measurement of the propulsion speed.

The results presented in Figure 2-8 reveal a downward trend for the non-dimensional velocity by greater than an order of magnitude (the physical velocity decreased from 10.3 ± 0.3mm/hr to 0.33 ± 0.03mm/hr). It is clear that the non-dimensional speed decreases with increasing angle everywhere, except for the change from the 2.5^o test to 5^o. This latter result is consistent with the known breakdown in the Phillips-Wunsch theory for small angles [16].

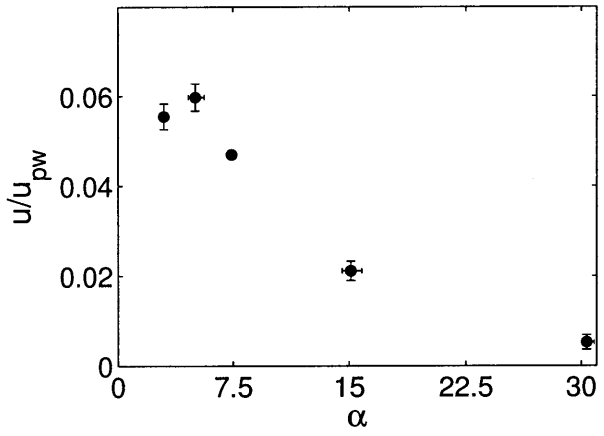

Figure 2-8: Plot showing the relationship between the non-dimensional velocity, $u/u_p w$, and the angle of the sloped walls of the wedge, α. Experiments were run using a NaCl-water mixture with a stratification of $d\rho/dz = -500\text{kg/m}^4$

2.4.3.2 Wedge Size

At this stage, an interesting prediction of dimensional analysis is that the propulsion speed is only a function of the aspect ratio, w/l, and not of the physical size of the object (since we have determined that the dimensionless speed is independent of Reynolds number and Froude number). To confirm this, we fabricate a 5cm long $\times$ 1.25cm wide wedge, which is a scaled version of the 10cm long $\times$ 2.5cm wide wedge used in all other parameter studies. In addition, wedges are manufactured with dimensions 18.10 $\times$ 2.50cm and 10.00 $\times$ 1.26cm, which have aspect ratios 0.138 and 0.126 respectively. Experiments are run with these four wedges using the standard experimental configuration of a 30 $\times$ 40cm tank filled with a NaCl stratification of strength $d\rho/dz = -500\text{kg/m}^4$.

The results of these experiments are presented in Figure 2-9. The two wedges with an aspect ratio of approximately 0.250 showed a percent difference in non-dimensional speed of 4%, while the two wedges of aspect ratio 0.138 and 0.126 have a percent difference in non-dimensional speed of less than 3%. These results reveal that, indeed, the size of the wedge plays a negligible role in setting the dimensionless speed. There is a potential limit to this result, however. If a wedge were to become

Width (cm)	Length (cm)	Aspect Ratio (w/l)	Area (cm^2)
5.00	3.01	1.661	15.03
2.51	3.10	0.810	7.76
1.26	5.04	0.250	6.34
2.49	10.05	0.248	25.03
2.50	18.10	0.138	45.32
1.26	10.00	0.126	12.59
1.26	19.90	0.0633	25.03

Table 2.3: Table of wedge dimensions, aspect ratios and projected areas.

so small that diffusion-driven flow was not able to fully develop, it is unlikely that it would be propelled at the same speed as a larger wedge. Furthermore, this relation may only hold at Reynolds and Froude numbers characteristic of this study.

2.4.3.3 Aspect Ratio Dependence

The final set of experiments concerns the influence of the aspect ratio, w/l, of the wedge on the propulsion speed. This is achieved by constructing several different wedges and running them in an otherwise identical system of a 30 $\times$ 40cm tank filled with a NaCl stratification of strength $d\rho/dz = -500\text{kg/m}^4$. In total, experiments are performed using five different wedges with a slope angle of 5^0, ranging in aspect ratio from 0.0632 to 1.661. The dimensions of all the wedges used are presented in Table 2.3. The limiting factors on the wedge width and length are the tank dimensions, as it is necessary to remain in the unconfined regime as determined by Section 2.4.1.

The aspect ratio results are presented in Figure 2-9. There is an upward trend for increasing aspect ratios, meaning the non-dimensional speed decreases as the wedge grows longer or narrower. Additionally, there is a significant difference between the extremums of the study (approximately 30%) which indicates that the aspect ratio must be considered when setting the non-dimensional speed.

The results presented in Figure 2-9 reveal a clear relationship between the aspect ratio and the non-dimensional velocity, demonstrating that a wider wedge goes faster. It is possible that this is related to the fact that as the wedge width grows, the diffusion-driven volume flux induced along the sloping walls of the wedge is increased.

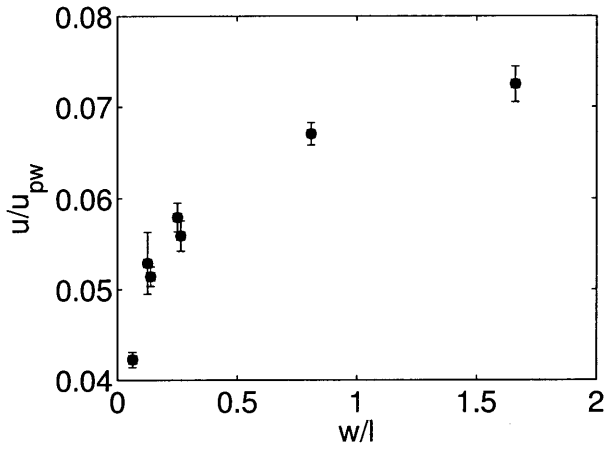

Figure 2-9: Plot showing the relationship between the non-dimensional velocity, $u/u_p w$, and the aspect ratio of the wedge, w/l. Experiments are run using an NaCl-water stratification of strength $d\rho/dz = -500\text{kg/m}^4$

By just changing the length of the wedge, however, there is no increase in the volume flux but there is expected to be an increase in the drag force experienced by the wedge.

2.4.4 Conclusions from Dimensional Analysis

This section has presented a dimensional analysis argument relating the non-dimensional velocity to its influencing parameters. The parameters are broken into three categories: confinement ratios, fluid properties, and wedge shape parameters. The confinement studies found that if the system is operating in the regime $L/l > 2$ and $W/w > 6$ then the dimensionless speed is not influenced by the tank size. Next, it is argued that the Reynolds and Froude numbers are changed by modifying the stratification strength, but this change does not impact the non-dimensional speed proving that these parameters can also be neglected from the dimensionless speed functionality. The Schmidt number is tested next by changing the stratifying agents and working fluid, but the change in dimensionless speed is less than 10% which reveals that this parameter can be neglected for this range of study.

Finally it is determined that only the wedge shape parameters influence the dimen-

sionless speed. The aspect ratio is varied through the use of different shaped wedges with the same slope angle, and the results of this variation are that as the wedge grows wider the non-dimensional speed increases. As the other shape parameter, the slope angle, is varied, the dimensionless speed peaks at an angles of approximately 5^o corresponding to the known breakdown of diffusion-driven flow [16].

2.5 Flow Visualizations

Having obtained a general understanding of the parameter space that governs the propulsion speed, the next focus is the flow structure around the wedge. Obtaining details of the flow structure around a moving wedge provides insight into the parameter dependences, allows for comparisons with the predictions of numerical simulations, and gives clear evidence that diffusion-driven flow is indeed present along the sloping walls of the moving wedge. As such this section presents the results of a series of experiments that measures the velocity field in the vertical and horizontal mid-plane of the moving wedge using Particle Imaging Velocimetry (PIV).

2.5.1 PIV Setup

PIV is a technique to measure the velocity field in a fluid by tracking the motion of neutrally buoyant particles [19]. The particles, hollow glass spheres of diameter $8 - 10\mu$m and density 1000-1200kg/m^3, float in the fluid and are illuminated by an Nd:YAG laser sheet. The laser is fired at set time intervals, a 4 megapixel camera images the illuminated particles in the illuminating plane of the laser sheet, and this data is saved for analysis. Once a sufficient number of images have been collected, cross-correlation software (DaVis 7.1) is used to locate small clusters of particles within subsequent images and determine the displacement of each particle cluster from one image to the next. By determining this displacement for a known time interval between laser pulses, a velocity field is readily computed.

For these experiments, the double bucket method [13] is used to fill the experimental tank with salt-stratified water, with particles added to facilitate the PIV

measurement. The particles are introduced into the double bucket system before filling and evenly distribute throughout the system due to the strong mixing processes inherent in the filling procedure. Once the stratification is established, the system is left for three days to allow the particles to settle to their neutrally buoyant positions throughout the tank. The experimental arrangement is such that for visualization in the horizontal mid-plane of the wedge, images are taken by a camera looking upwards through the bottom of the tank. Therefore, during the settling process a plate covers a portion of the base of the tank, collecting any particles that settle to the bottom. Once the settling process is complete, this plate is slowly moved out of the way, leaving a window on the bottom of the experimental tank that is free from particles, providing a clear view into the tank for the camera.

With the stratification established, the PIV camera and laser are used to make PIV measurements. The laser sheet can be oriented to cut through either the horizontal or vertical mid-planes of the wedge, while the position of the camera is accurately controlled by mounting it on a pair of translation stages. This traverse system is mounted to the side of the experiment in order to image the vertical mid-plane of the wedge, or is mounted beneath the tank to obtain horizontal mid-plane images.

In a typical experiment, the wedge is released using the cage-release mechanism and then an hour passes to ensure that all transients are eliminated. Because the scale of the boundary layer flow adjacent to the wedge is on the order of a millimeter, it is necessary to get the highest resolution images possible, which is a 2.5cm square region, in order to resolve this flow. A single data set for each 2.5cm region consists of sixty images taken at a frequency of 0.25 Hz, this frequency being determined by the slow flow speeds. After a data set is collected, the camera moves on the traverse system to take images for the next flow-field location. To capture the complete flow field around the wedge, a three-by-ten grid of images is collected in both the vertical and horizontal mid-planes, with the position of the camera and the time of imaging carefully documented to determine the exact position of the camera relative to the moving wedge.

2.5.2 PIV Results

The results of the PIV experiments for a wedge moving at 2.3×10^{-6}m/s in a stratification of $d\rho/dz = -350\text{kg/m}^4$ are presented in Figure 2-10. The vertical mid-plane velocity field (Figure 2-10a) shows a strong boundary layer flow along the upper sloping walls of the wedge, and a slower bulk flow extending about 4cm further above this. This strong boundary layer flow (10^{-5}m/s) is consistent with the magnitude of diffusion-driven flow predicted by the analytical model (eq. 1.15). Other flow features in the vertical mid-plane are; a strong incoming jet that supplies fluid to the boundary layer flow, and so-called blocked flow behind the wedge (i.e. the fluid immediately behind the wedge moves as a rigid body with the wedge). This blocked flow behind the wedge is a commonly occurring phenomenon for a slowly moving object through a stratified fluid [3].

The horizontal mid-plane velocity field (Figure 2-10b) shows the interesting feature that fluid is drawn into both the front and rear of the wedge, and this flow extends at least 8cm to the side of the wedge. This result reveals that the flow extends out to the sides much further than it does in front or behind the wedge, which provides a basis for understanding why the width ratio of the wedge must be much larger than the length ratio in order for the wedge to behave as if it is unconfined, as is found in Section 2.4.1. With fluid being drawn in towards the wedge from all directions in the horizontal mid-plane there must be locations where the fluid is expelled from the wedge that are not captured in our visualizations, indicating that the flow field has a complex three-dimensional structure.

2.6 Numerical Simulation

With a basic understanding of the flow field established, we now seek to investigate the pressure-field and density-field perturbations due to diffusion-driven flow, in an effort to understand the nature of the propulsion force on the wedge. This is pursued using a numerical simulation. Two-dimensional simulations run using COMSOL reveal significant modification to the boundary layer density stratification, but the flow

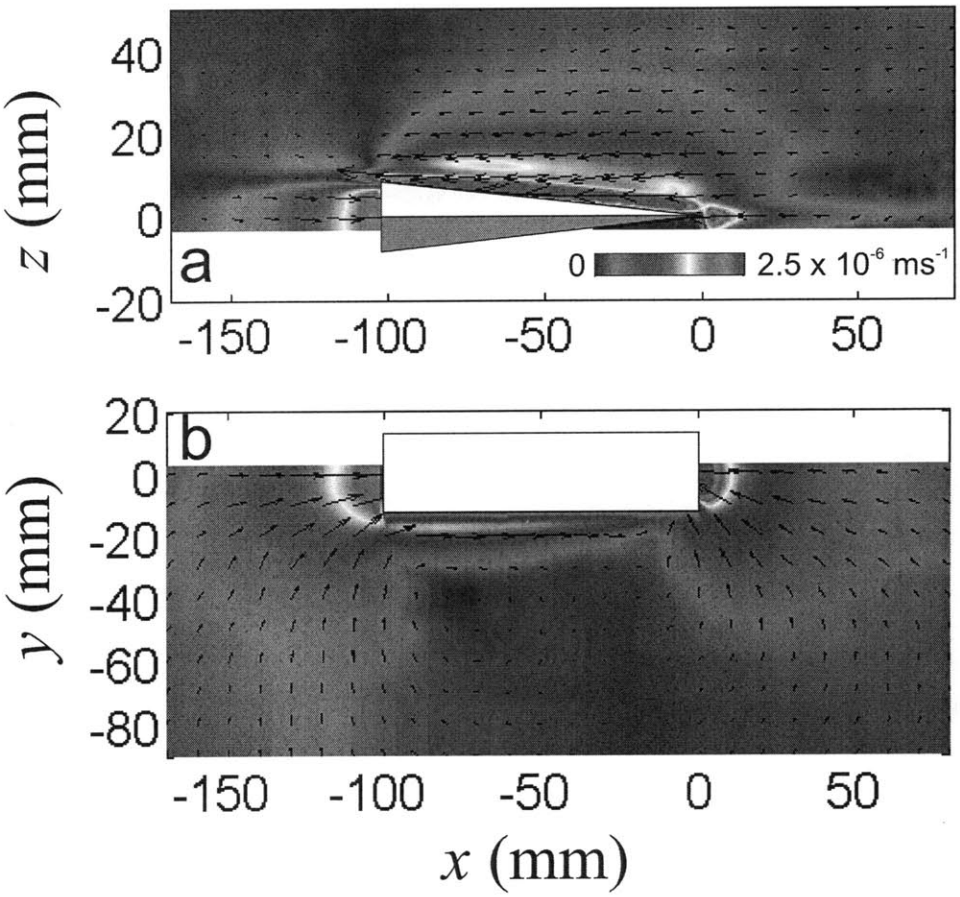

Figure 2-10: Composite flow fields for the (a) vertical mid-plane and the (b) horizontal mid-plane of the wedge moving at speed 2.3×10^{-6}m/s in a stratification of $d\rho/dz = -350\text{kg/m}^4$. The color scale saturates lower than the peak velocity (10^{-5}m/s) to emphasize flows outside the boundary layer.

visualizations indicate that the phenomenon is highly three-dimensional problem, requiring three-dimensional simulations. These three-dimensional simulations were run by Dr. Mike Barad at Stanford University.

2.6.1 Simulation Configuration

Simulations are run using a Franklin (a Cray XT4) supercomputer via a code using an adaptive, block-structured, two-way nested, second-order accurate finite-volume approach to solving a fluid system with variable density [4]. The system parameters used in the three-dimensional simulation, selected to model a typical experiment, are a wedge measuring 98.35mm long, 25.00mm wide, and an angle of inclination of 5°,

and a 300mm cube domain filled with water. With an origin at the bottom rear corner of the cube, the wedge is positioned with its front tip centered at (170, 150, 150)mm. Due to numerical convergence issues, a thermal stratification rather than a NaCl stratification is used, meaning a diffusion coefficient of $\kappa = 10^{-6}\mathrm{m}^2/\mathrm{s}$ and a kinematic viscosity of $\nu = 10^{-6}\mathrm{m}^2/\mathrm{s}$, resulting in a Schmidt number of 1, are used. The density gradient used is $d\rho/dz = -546\mathrm{kg}/\mathrm{m}^4$ with a centerline (and wedge) density of $\rho_o = 1105\mathrm{kg}/\mathrm{m}^3$.

The mesh consists of three different levels of cubes, where sizes vary to provide different levels of accuracy for different regions of the flow field. The course mesh, of size 2.34375mm, fills the system above and below the horizontal layer of the fluid containing the wedge. The mesh size is reduced by a factor of two in the horizontal layer containing the wedge. Finally, in the region immediately around the wedge, the scale of the mesh is halved again to 0.5859375mm. With this resolution there are approximately ten mesh points in the characteristic boundary layer thickness, which is expected to be about 5mm wide; a salt-stratification boundary layer would be less than 1mm thick, requiring a higher resolution mesh to resolve.

The governing equations and the boundary conditions are the final component of the simulation. The equations used are the continuity (eq. 1.5), incompressible Navier-Stokes (eq. 1.6), and diffusion equations (eq. 1.7). No-slip boundary conditions (eq. 1.11) are applied at all surfaces, including the wedge, and a constant pressure is applied on the uppermost boundary of the system. The diffusion boundary condition used is a no-flux condition (eq. 1.12) along all boundaries, except the top and bottom of the system, which are set at constant densities to prevent density-gradient decay. Finally, the wedge is stationary in these simulations because an adaptive mesh is a major challenge for the code that could not be readily implemented.

2.6.2 Simulation Results

The first step in the data analysis is to determine if the system has reached a steady state. The evolution of the system is tracked by calculating the total kinetic energy

of the flow field, i.e. the sum of kinetic energy using all mesh points through the volume. To confirm that steady state has indeed been reached, the evolution of the force on the wedge is also checked; the method behind this calculation is described in the next section. Once both these quantities reach a value that varies by less than 1% over time, it is concluded that the system has reached steady state.

After the simulation has reached steady state, it is then possible to analyze the velocity field. Figure 2-11 presents results for the horizontal velocity field, density perturbation field, and pressure perturbation field. The velocity field, presented in Figure 2-11a, displays a number of similar characteristics to the PIV flow visualization, presented in Figure 2-10. For example, there is a strong boundary layer flow along the sloping wall, as well as a slower bulk flow in a lobe shape above the wedge, and there exists a strong incoming jet at the tip and a pair of rear jets. A couple of understandable differences are that no blocking flow exists in the simulation because the wedge is stationary, and the velocities in the simulation ($\sim 10^{-3}$m/s) are greater than in the experiments ($\sim 10^{-6}$m/s) due to the higher diffusivity in the simulation. Overall, however, there is excellent qualitative agreement between experiment and numerics.

The plot in Figure 2-11b reveals the difference between the density field in the presence of diffusion-driven flow and the unperturbed linear density stratification initially present. There is a clear layering of density perturbations ranging between ± 0.2kg/m^3 above and below the wedge. The density perturbation above the upper sloping surface of the wedge shows a slight decrease from the far field and the density perturbation below the lower sloping wall of the wedge reveals a density that is slightly higher than the far field value. This result is in agreement with the theoretical predictions by Woods that diffusion-driven flows in a finite domain will influence the local density field [27].

The pressure field perturbation, presented in Figure 2-11c, is the total pressure field in the presence of diffusion driven flow minus the pressure directly behind the wedge, where there is no flow present. This analysis reveals a pressure drop ($\sim$ 8mPa) along the sloping surfaces of the wedge. The hydrostatic pressure of the simulated

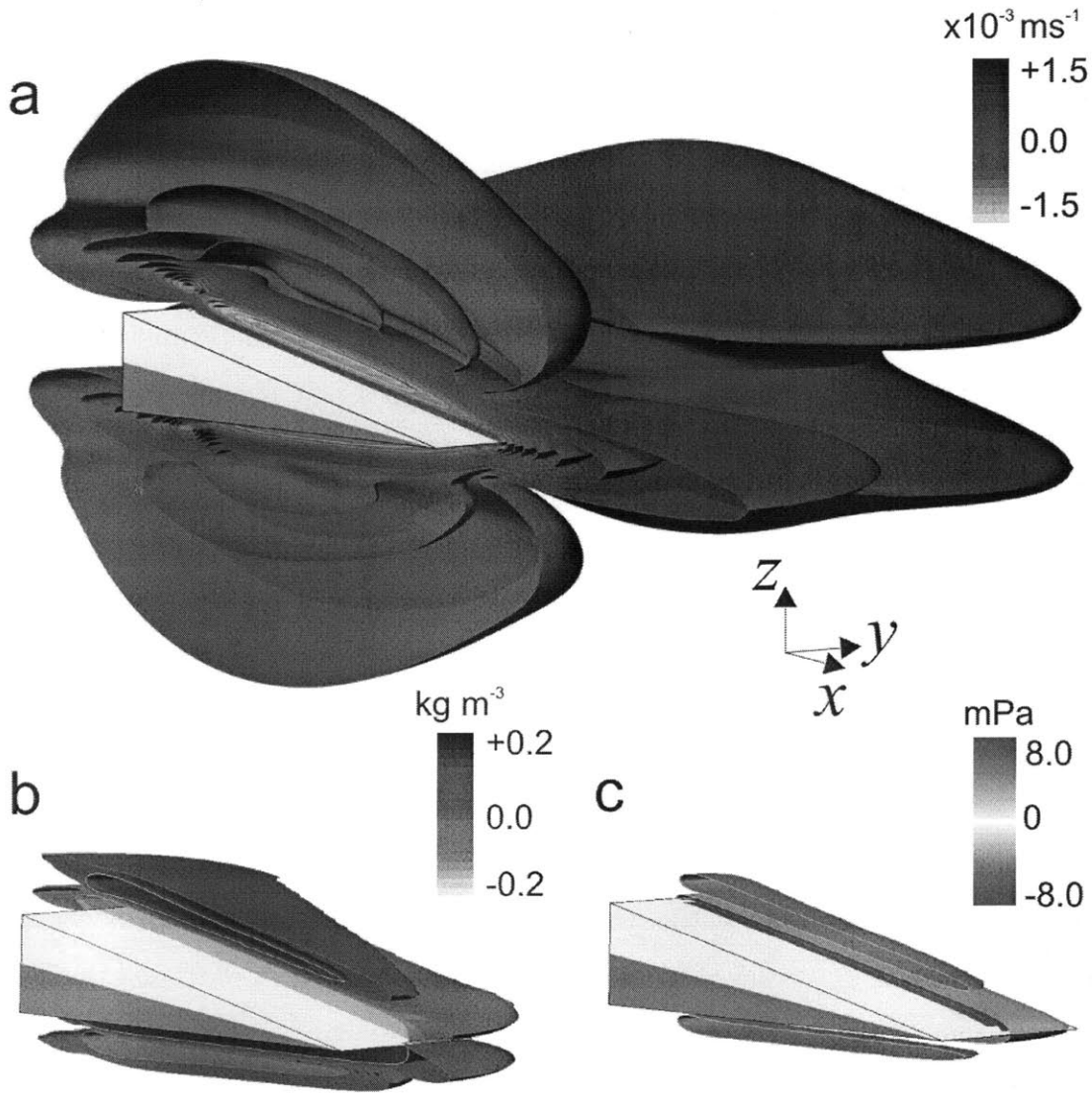

Figure 2-11: Isosurfaces developed from the Stanford simulations (a) velocity field (b) density perturbation from bulk (c) pressure difference from rear of wedge.

density field completely accounts for the pressure field including the perturbation, indicating that all pressure perturbations are due to density perturbations and are not influenced by dynamic effects. With a negative pressure perturbation on its sloping surfaces, the wedge feels a net force forward created by the higher pressure on its rear.

These results reveal a picture that the induced velocity field affects the density distribution around the wedge, which in turn impacts the hydrostatic pressure distribution over the surface of the wedge. In the semi-infinite case studied by Phillips [17], this pressure drop is balanced by the viscous drag, but here the situation is not as simple because the system is three dimensional and requires return flows outside the boundary layer. It therefore remains to determine the net thrust on the wedge, which is the subject of the next sub-section.

2.6.3 Force Calculation

Using the numerically-calculated pressure and density perturbations, the propulsion force on a stationary wedge is determined. Since the wedge is fixed in the simulation, a reasonable estimate of the propulsion speed of this wedge, were it free to move, is to balance the calculated propulsion force with a low Reynolds number viscous drag. Here, we describe the methods for calculating the propulsion force and the expected drag on the wedge.

A standard method of calculating force on an object is to calculate the total shear and pressure forces on the surface of the wedge. This method requires precise and high-resolution data over the entire surface of the object. However, this is not reasonable for the type of mesh used in this simulation as the mesh is not aligned with the sloping surfaces making it difficult to accurately calculate velocity gradients. An alternative method for calculating the force on the wedge is through the use of a control volume that completely contains the wedge [5]. This approach is based on the integral relation:

$$\sum \underline{F}_{tot} = \frac{d}{dt} \int \rho \underline{q} dV + \int \rho \underline{q} (\underline{q} \cdot \hat{\underline{n}}) dS \tag{2.6}$$

where $\underline{F}_{tot}$ is the total force on the control volume V bounded by the surface S with an outward normal unit vector $\hat{\underline{n}}$. Equation (2.6) states that the total force on the control volume is balanced by the sum of the rate of change of momentum within the volume and the net momentum flux into the volume. This total force can be decomposed into three components:

$$\sum \underline{F}_{tot} = -\int p\hat{\underline{n}}dS + \int \underline{\underline{\tau}} \cdot \hat{\underline{n}}dS + \underline{F}_{wedge} \tag{2.7}$$

where p is the pressure, $\underline{\underline{\tau}}$ is the stress tensor, and $\underline{F}_{wedge}$ is the body force imposed by the wedge on the fluid. This study is only interested in horizontal forces, so the calculation is only performed for the coordinate aligned with the wedge length.

The control volume calculations are performed using Matlab. The code allows the user to select the control volume location and the grid size for the surfaces of the control volume. With these settings, the Matlab code calculates the force components and the momentum fluxes and forces for each surface of the control volume. The shear stress requires the calculation of the velocity gradient, which is determined using the fourth-order center-divided derivative equation:

$$f(x_i) = \frac{-f(x_{i+2}) + 8f(x_{i+1}) - 8f(x_{i-1}) + f(x_{i-2})}{12h} + O(h^4), \tag{2.8}$$

where $f(x)$ is a function for the discrete variable x with indices i and step size h. To calculate the surface integrals, the following Simpsons integration technique is used:

$$\int_a^b f(x)dx = (b-a)\frac{f(x_0) + 4f(x_1) + f(x_2)}{6} - (1/90)h^5 f^{IV}(x). \tag{2.9}$$

Once the force components are calculated they are summed together to give the force on the control volume. To check the accuracy of these numerical schemes, tests were performed for pressure driven flow and Couette flow in a channel, yielding results with better than .01% accuracy. The results obtained using this approach also agree well with test results using the surface force routine in COMSOL.

Using the control volume approach, the estimate of the force acting on the wedge

for the configuration described in Section 2.6.1 is $F_{wedge} = 4.3 \times 10^{-7}$N, and the direction of propulsion force is forward, toward the tip, in accord with the experimental result. To ensure that the force calculations are reliable, multiple volumes are used in calculating this force and the result changes by at most five percent while changing the volume by a factor of four. The reason for this small variation is likely due to the numerical noise present within the simulation.

In the experiment, since the wedge moves at constant velocity, it must be that the propulsion force is balanced by a drag force. To determine if the propulsion force calculated is consistent with our experimental results, we seek to estimate a drag force on the wedge. The challenge is, however, that there are no published results for the drag force on an object moving slowly and horizontally through a stratified fluid. To address this shortcoming, a COMSOL simulation is used to calculate the drag of unstratified fluid on the wedge, and it is assumed that while stratification will enhance this value somewhat, the magnitude of the drag will still be of the same order [24]. The resulting velocity is $u = 4.5 \times 10^{-4}$m/s, which corresponds to a non-dimensional velocity of $u/u_{pw} = .02$ that compares favorably with the experimental value of 0.06. Overall, this analysis supports the belief that the propulsion of the wedge occurs because diffusion-driven flow manipulates the hydrostatic pressure field around the wedge via density field perturbations.

2.7 Conclusions and Future Works

A number of interesting and novel results have been discovered in this study. The most substantial result is that an asymmetric object with sloping walls will spontaneously project itself through an otherwise quiescent, stratified fluid. This result is clearly demonstrated experimentally by comparing the motion of the wedge and a sphere.

To better understand what determines the propulsion speed, a parametric study was performed. This study found that it is possible for an object to move as if unconfined provided the system is large enough, and that the dimensionless propulsion speed is only a function of the geometry of the object. PIV methods were used to

visualize the flow structure around a moving wedge and these results were qualitatively reproduced in a three-dimensional numerical simulation. Finally, analysis of the numerical data revealed that propulsion occurs because the density field around an object is perturbed by the induced diffusion-driven flow, resulting in a pressure drop along the sloping surface of the object driving it forward.

Building on this discovery, there are a number of different avenues that can now be pursued. One interesting possibility is to study how floating objects can interact via the diffusion-driven flows they produce. A preliminary experiment reveals that the presence of one wedge can modify the speed and trajectory of another, as shown in Figure 2-12. Another scenario is to determine if it is possible to rotate an object due to diffusion driven propulsion. With the use of a configuration similar to the one shown in Figure 2-13, perhaps it would be possible for the two wedges to rotate about a central point. This arrangement would create a moment about the central point due to the forces on each wedge induced by diffusion-driven flow, resulting in a constant rotation of the double wedge system.

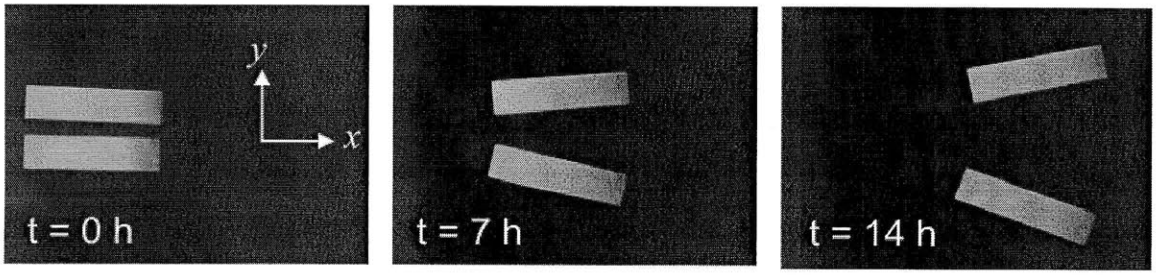

Figure 2-12: Time stamped images of two wedges released in the same orientation side by side.

Another avenue of research is to study whether objects can be propelled by surface heating and cooling. The motivation for this is the recognition that diffusion-driven flow has a close connection with the problem of valley winds studied by Prandtl [18]. We have constructed a floating inverted wedge, which is shown in Figure 2-14. The idea is that by heating the fluid under one of the sloping walls, a buoyancy driven force will drive fluid upwards along the wall and create a pressure increase. Both

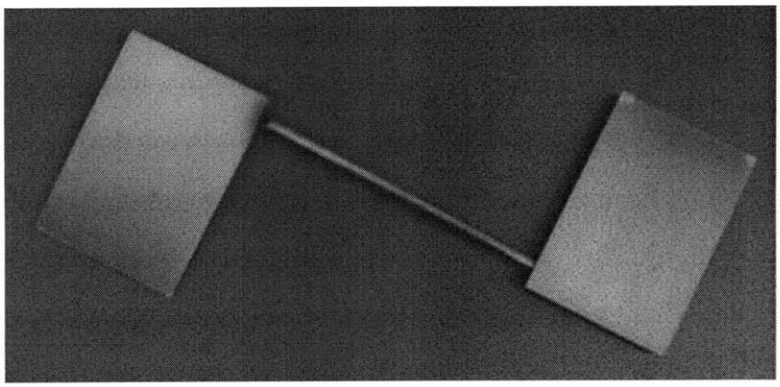

Figure 2-13: Two wedge of width 3.5cm connected by a hollow aluminum rod.

shear and pressure forces will act on the wedge in opposite directions and remains to be determined whether one of these forces can dominate the other, producing thrust. Since these flows are much stronger than diffusion-driven flow, however, it might be that the propulsion speed is significantly faster for this scenario.

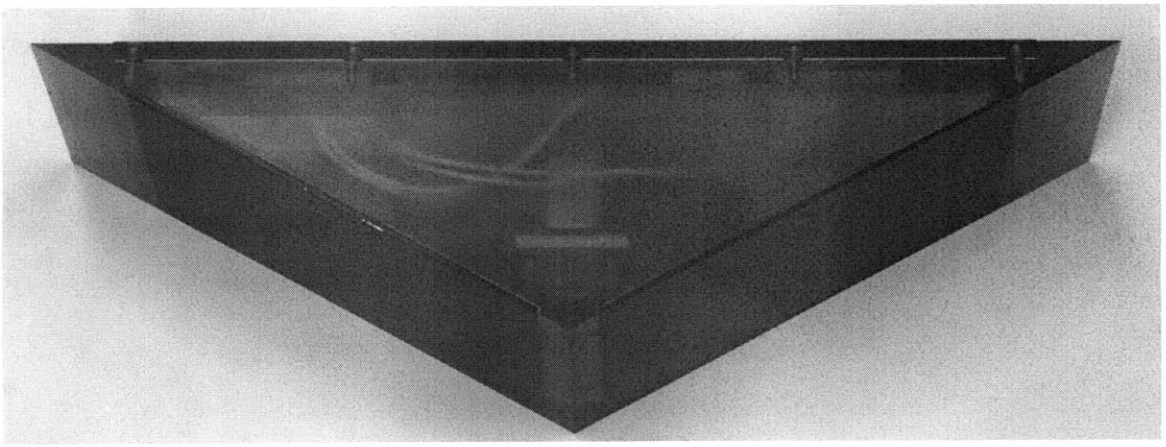

Figure 2-14: Heated wedge 26cm long. Electronics contained inside with heaters on the sloping walls.

Chapter 3

Measuring Molecular Diffusivity

Molecular diffusivity is a measure of the rate at which a solute diffuses in a solution. This property is very important in a number of applications ranging from double-diffusive research to drug delivery [21] [22]. Currently there are a few established ways to measure molecular diffusivity, but each method has its limitations. This chapter presents a novel method of measuring the molecular diffusivity that overcomes some of the shortcomings of previous methods. The measurement concept exploits established analytical results for the volume flux resulting from diffusion-driven flow. Along with a description of the measurement technique, the results of a series of numerical studies are presented to demonstrate the validity of the method. Finally, a proof of concept experiment is run and the results from these experiments are also presented.

3.1 Existing Measurement Methods

Researchers have sought methods to rapidly and accurately measure the molecular diffusivity of solutes in solutions. There are two principal methods that are currently employed as standard techniques for this measurement: the diaphragm technique [23] and the interferometric method [1]. A few other methods have also been investigated, and these are reviewed by Tropea *et al.* [25].

The diaphragm method of measuring molecular diffusivity [23] uses two solutions,

one containing the solute whose molecular diffusivity is to be determined and the other being solute free. The two solutions are stored in a container in which they are separated by a porous diaphragm of known thickness; this allows diffusion between the two solutions while minimizing the influence of convection. To maintain uniform concentrations on either side of the diaphragm, the solutions are constantly mixed by a magnetic stirrer that prevents a layer of different concentration forming adjacent to the diaphragm. During a run time of several hours, the concentration in the previously solute-free solution is measured, and this concentration as a function of time enables calculation of the diffusion coefficient.

While the diaphragm technique has been widely utilized, it possesses several drawbacks. The most crucial issue is that this method measures the diffusion coefficient between two distinct concentration levels as opposed to measuring molecular diffusivity for a particular concentration. Another concern is that the mechanical stirring rates on either side of the diaphragm could still have an influence on the result. The run time for obtaining data is also quite long (i.e. several hours), and it is necessary to maintain constant environmental conditions throughout this entire time. Finally, the concentration is typically determined by measuring the electrical conductivity of the fluid, which requires a sensitive and accurately calibrated conductivity probe.

The interferometric method of measuring molecular diffusivity exploits the relationship that exists between the solute concentration and the index of refraction of a fluid [1]. In this approach, a cell contains two layers of fluid, the lower of which contains the solute for which the molecular diffusivity is being determined. The system is allowed to diffuse naturally, and periodically during the run an interferometer measures the refractive index of the fluid at a number of vertical locations, creating a refractive index profile as a function of time. Assuming that the refractive index is proportional to the solute concentration, the measured refractive index evolution can be converted to a concentration evolution, which is fitted to a theoretical prediction that uses the molecular diffusivity as a fitting parameter. The value of the molecular diffusivity that provides the best fit to the experimental data is then taken as the measurement result.

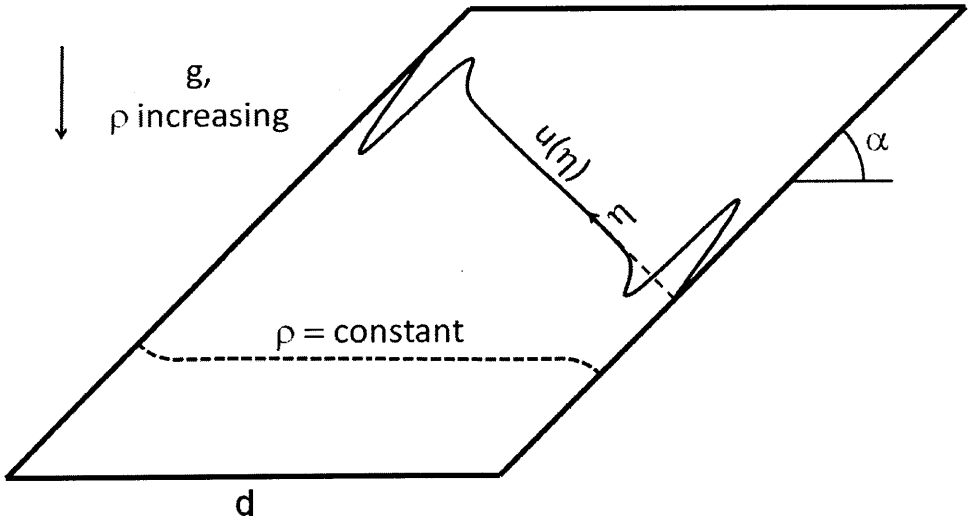

Figure 3-1: Sketch of the tilted fissure system.

There are also several issues with the interferometric method of measuring molecular diffusivity. As in the diaphragm technique, the interferometric method is most accurate for diffusion of one solution into another and it is necessary to maintain system parameters for a number of hours. Convection is of even greater concern in this method as there is nothing present in the system to suppress convection. Finally, the optical arrangement for the interferometric method is quite non-trivial and specialized.

3.2 A Novel Measurement Concept

Phillips [17] considers diffusion-driven flow in a fissure, for which the configuration is an infinitely long channel with parallel walls at an angle α with respect to horizontal and a distance d apart. The system contains a linearly stratified fluid with a density gradient $\partial\rho/\partial z$ and the dynamic viscosity of the fluid is μ. A schematic of the configuration is presented in Figure 3-1, which also shows a sample velocity profile, $u(\eta)$, as a function of the wall-normal coordinate, η, and an example isopycnal, albeit in a fissure of finite length.

In the analytical solution obtained by Phillips [17], the velocity and density perturbations exist in thin boundary layers of characteristic width $1/\gamma$ (eq. 1.16) adjacent

to each of the sloping walls. For a system that is much wider than these boundary layers (i.e. $1/\gamma \ll d$), the boundary layer flows and density perturbations along the two sloping walls are essentially independent of each other. As is the case for the diffusion-driven flow profile for a semi-infinite system (eq. 1.15), the net volume flux along each of the sloping walls is

$$Q = \kappa \cot\alpha. \tag{3.1}$$

Again, it is noted that this volume flux is independent of the density, density gradient, and viscosity. For the finite domain presented in Figure 3-1, the flow up along one wall and down the opposite wall induces a counter-clockwise flow direction, with cross-flows at the top and bottom of the fissure.

In developing a new experimental method to measure molecular diffusivity, we exploit the fact that the volume flux, Q, of the boundary layer flows in a wide fissure is only a function of the molecular diffusivity and the slope angle. Provided this volume flux can be measured and the slope angle is known, the molecular diffusivity can be readily determined. The challenge, therefore, is to make reliable measurements of the volume flux, which requires making measurements of the velocity field.

A standard technique for making velocity field measurements is Particle Image Velocimetry (PIV), which was the technique used to investigate the flow field around the moving wedge, as described in Chapter 2. For the case of flow in a fissure, one challenge for making PIV measurements is that it is typically very difficult to get reliable velocity field data near a surface due to laser glare. As such, we consider the system presented in Figure 3-2. This chevron shaped system mirrors the fissure studied by Phillips [17], in that diffusion-driven flow exists along the slanted walls, but in this configuration the cross-flows traverse the bulk, away from any boundaries. Furthermore, the cross-flow at the center of the chevron has twice the volume flux along an individual sloping boundary, since it must supply two diffusion-driven flow boundaries, making the flow stronger and easier to detect. This central cross-flow is where it is proposed to measure the volume flux and thus determine molecular

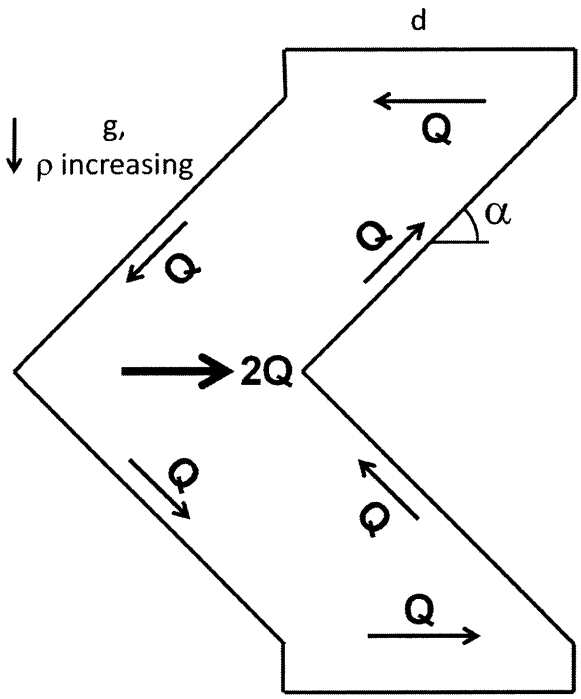

Figure 3-2: Chevron system used to measure the molecular diffusivity. A volume flux of Q circulates in the top half and bottom half of the system, as shown.

diffusivity.

The proposed measurement technique makes it readily possible to explore how molecular diffusivity is influenced by a range of parameters. The density stratification in the system persists all the way from the lower reservoir, up through the chevron, to the upper reservoir, and so by raising and lowering the stratification with respect to the chamber it is possible to arrange for a particular concentration to be present at the tip of the chevron. Thus one can measure the molecular diffusivity for a particular concentration, rather than measuring molecular diffusivity for a discrete jump in concentration, as in other methods. It is also possible to study any effects the viscosity, density gradient, and temperature have on the molecular diffusivity.

3.3 Numerical Studies

To aid in the design of an experimental apparatus, and to test the proposed measurement method, several numerical simulations were run using COMSOL. The sim-

ulations use the incompressible fluid dynamics and diffusion packages. The first goal is to create a system where the simulated flows match those predicted by Phillips [17]. Thereafter, a parameter study is performed to ensure that the volume flux relationship (eq. 3.1) holds true for a variety of system parameters.

3.3.1 Simulation System

The COMSOL simulation uses the governing equations from fluid dynamics and diffusion to calculate velocity and density fields for a given geometric configuration and boundary conditions. The governing equations for the simulation are

$$\underline{\nabla} \cdot \underline{q} = 0, \tag{3.2}$$

$$\rho \frac{\partial \underline{q}}{\partial t} + \rho(\underline{q} \cdot \underline{\nabla})\underline{q} = -\underline{\nabla} p + \mu \nabla^2 \underline{q} + \rho \underline{g}, \tag{3.3}$$

$$\frac{\partial \rho}{\partial t} + \underline{\nabla} \cdot (-\kappa \underline{\nabla} \rho) = -(\underline{q} \cdot \underline{\nabla})\rho, \tag{3.4}$$

where ρ is the density, μ the dynamic viscosity of the fluid, $\underline{q}$ the velocity field, p the pressure, $\underline{g}$ the gravity vector, and κ the molecular diffusivity. Equations (3.2) and (3.3) define the fluid mechanics and are the continuity and Navier Stokes equations respectively, and diffusive processes are governed by the convection-diffusion equation (eq. 3.4).

Due to the vertical symmetry of the configuration in Figure 3-2 (i.e. it is symmetric about the horizontal centerline), it is possible to consider only the top half of the chevron and use a symmetry condition at the mid-plane. The domain of the simulation is shown in Figure 3-3. To confirm the validity of using only the half domain, several simulations were run using the full chevron configuration and the results were compared with the half-domain simulations, with excellent agreement.

The two main components of the simulation system are the mesh and the boundary conditions that must be applied to the governing equations (3.2-3.4). The overall system is decomposed into several distinct regions, as indicated in Figure 3-3. Along the two side walls highlighted in pink, a no-flux, no-slip boundary condition is applied.

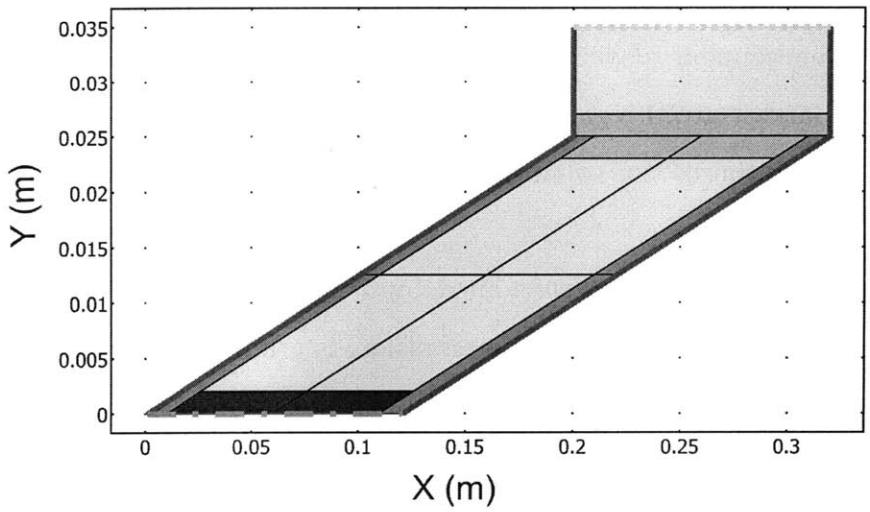

Figure 3-3: Simulation system. High mesh density corresponds to a darker green fill and a low mesh density corresponds to a pale green fill. The side walls shown in pink are no slip, insulating boundaries. The top boundary (dotted yellow) is an open boundary at constant concentrations, and the bottom boundary (dashed orange) is a symmetry boundary at constant concentration.

At the top of the system, indicated by a yellow dotted line, an open boundary sets the pressure of the system and a constant concentration boundary condition is applied. Finally, a symmetry condition is applied for the fluid dynamics solver and a constant concentration condition is used for the diffusion solver at the bottom boundary of the system, indicated by the orange dashed line. The reason the top and bottom boundaries of the system are set at constant concentration is to ensure a time independent stratification throughout the domain.

The limiting resource in these simulations is the computer memory, which constrains the number of mesh points that can be used. To cope with this, the mesh has four different levels of refinement for different regions of the flow field. In the bulk (the pale green region in Figure 3-3), there is essentially no flow occurring, so there is no need to have a highly refined mesh in this region; this is also the case for the reservoir at the very top of the system. The horizontal cross-flow at the top of the chevron (the turquoise region in Figure 3-3) has the next lowest mesh density, since there is a weak flow occurring here which is never analyzed. The second highest mesh concentration (the dark green region in Figure 3-3) is along the sloping walls, since it

is important for there to be an accurate simulation of the diffusion-driven flow that occurs in a fine boundary layer along these sloping walls. Finally, the highest mesh density (the darkest green region in Figure 3-3) is in the bottom cross-flow section, where the calculation of the volume flux to be measured occurs and the simulation must be very accurate.

The size of the system is determined by a number of tests. It was discovered that for a given set of physical parameters there is a minimum gap thickness for the cross-flow jet at the lower boundary to fully develop. This is because the cross-flow suffers from sidewall influences as the direction of the flow is drastically changed when transitioning from a boundary layer flow to a cross-flow. More specifically, the gap thickness required for the cross-flow to become fully developed, by which it is meant that the volume flux in the horizontal cross flow becomes independent of horizontal position, is a function of the boundary layer size. It is also important to ensure that the system is sufficiently tall that the expected boundary layer flow is achieved on both sloping boundaries.

A sample simulation result is presented in Figure 3-4. The parameters used for this simulation are: $\kappa = 10^{-9}$ m^2/s, $\mu = 10^{-3}$ Pa·s, and $d\rho/dz = -10^2$ kg/m^4. The slanted region is 0.125m wide and 0.025m tall at an angle of 7.1^o. The mesh has the following element densities: 695, 523, 269, 72 elements per square millimeter, totaling 741732 elements. After a run time of about one hour and a half, the simulation converges to the velocity field (Figure 3-4) and the density profile. The result shows strong diffusion-driven flow restricted to the boundary layers along the sloping walls. At the top of the system a broad cross-flow transports fluid from one slanted boundary to another, while at the bottom, a much narrower jet returns the fluid from left to right. There is no flow throughout the center of the system, as expected, and there is also no flow in the reservoir at the very top of the system.

3.3.2 Numerical Confirmation of Phillips Solution

The first results are a comparison between the analytical profile of Phillips profile [17] and the results of the numerical simulation. The analytical solution of Phillips

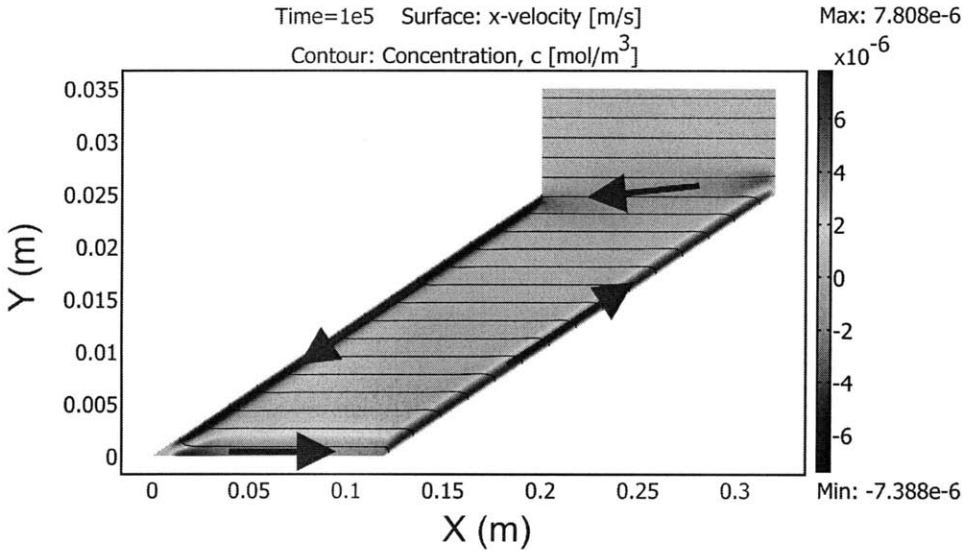

Figure 3-4: Plot of the x-velocity magnitude and constant concentration lines. Arrows are added to indicate direction of the flow.

is as follows. With the origin midway between the two walls of a fissure and the wall normal coordinate being η, the unidirectional flow profile, $u(\eta)$, in the fissure is

$$u(\eta) = \frac{g\cos\alpha\sin\alpha}{2\gamma^3\mu}\frac{d\rho}{dz}\left(-F\cos(\gamma\eta)\sinh(\gamma\eta) + G\sin(\gamma\eta)\cosh(\gamma\eta)\right), \tag{3.5}$$

where

$$F = \frac{\sin(\frac{\gamma d}{2})\cosh(\frac{\gamma d}{2})}{\sin(\frac{\gamma d}{2})\cosh(\frac{\gamma d}{2}) + \cos(\frac{\gamma d}{2})\sinh(\frac{\gamma d}{2})},$$

and

$$G = \frac{\cos(\frac{\gamma d}{2})\sinh(\frac{\gamma d}{2})}{\sin(\frac{\gamma d}{2})\cosh(\frac{\gamma d}{2}) + \cos(\frac{\gamma d}{2})\sinh(\frac{\gamma d}{2})}.$$

A comparison between numerical results and the Phillips profile (eq. 3.5) is presented in Figure 3-5. The parameter values for this simulation are the same as for the simulation presented in Figure 3-4, with the exception of $w = 0.025$ m and $\alpha = 26.5^o$. Three velocity profiles have been extracted from the simulation data in Figure 3-5(a), and the numerical results are directly compared with the analytical profile in Figure 3-5(b). In addition, the difference between simulation and theory is plotted in Figure 3-5(c). The characteristic difference is on the order of 1%, revealing that the analyti-

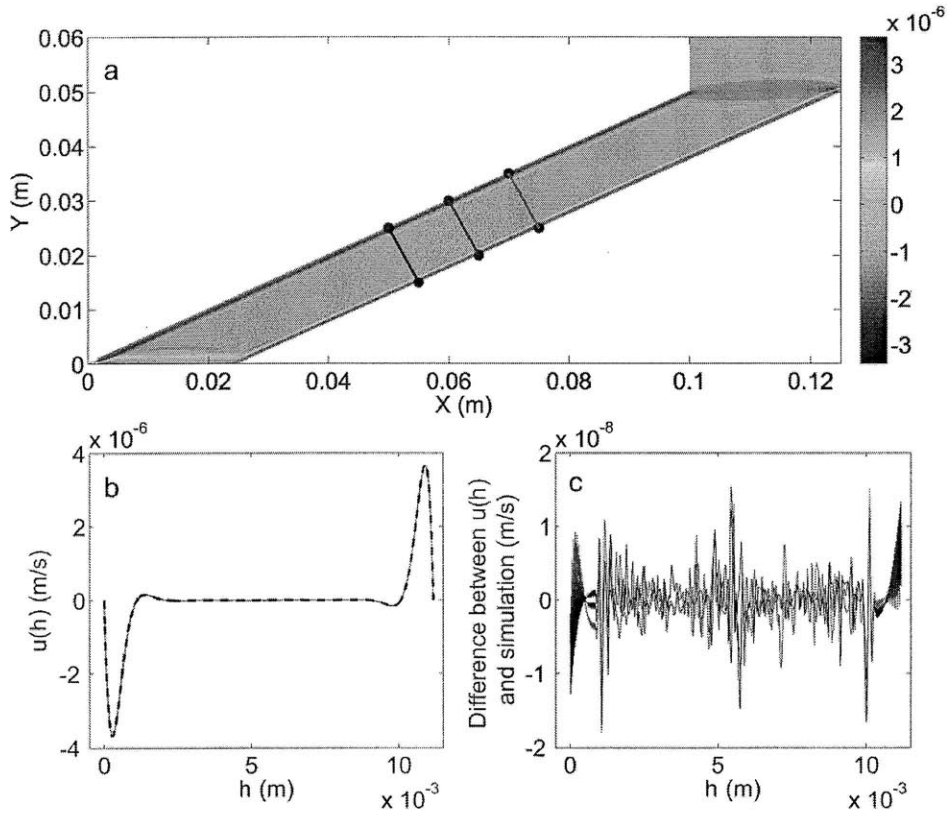

Figure 3-5: A comparison of the velocity profiles in the simulation with the theoretical prediction of Phillips (eq. 3.5). (a) Simulation data for the horizontal velocity and markers for where the data is being interpolated. (b) Velocity profiles for the three interpolated segments and the Phillips model (dashed line). (c) Plot of the difference between the Phillips model and the simulation data.

cal solution is achieved by the simulation, making it possible to proceed with volume flux calculations.

3.3.3 Numerical Parameter Study

Having established the validity of the numerical solution in the half-chevron domain, it is now possible to proceed to investigate how, and if, various parameters influence the cross-flow volume flux at the lower boundary. Theoretically, the only two contributing factors should be the molecular diffusivity and the angle of inclination of the walls. To confirm this, we vary the density gradient, dynamic viscosity, and the width of the chevron. In order to calculate the volume flux, Simpson integration [7] is used to numerically integrate the horizontal velocity across the lower cross-flow jet.

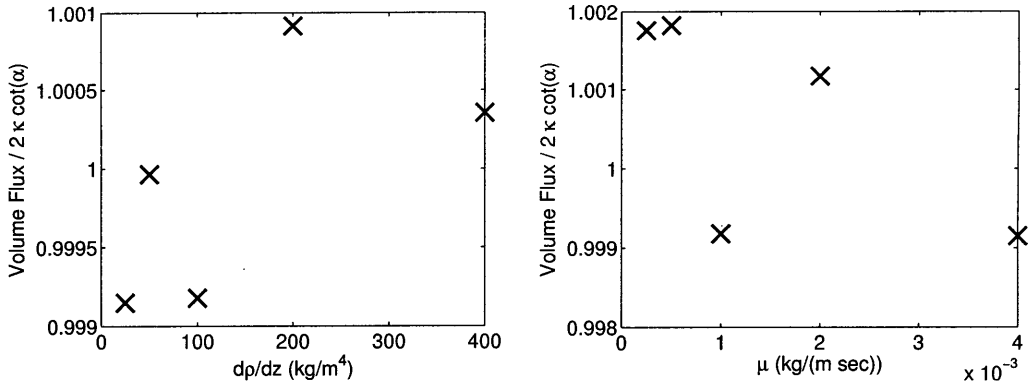

Figure 3-6: (a) Plot of the comparison between the simulated and the theoretical volume flux as a function of the density gradient. (b) Plot showing how the viscosity changes the volume flux for the simulation.

The first tests determine the impact of independently varying either the density gradient or the viscosity while all other parameters are held constant. The density gradient is varied from $d\rho/dz = -25$ kg/m^4 to $d\rho/dz = -400$ kg/m^4, and the dynamic viscosity is varied from 0.25×10^{-3}kg/m/s to 4×10^{-3}kg/m/s. The other (fixed) parameters used in these simulations are $\kappa = 10^{-9}$ m^2/s, $w = 0.025$m, $\alpha = 26.5^o$, $\mu = 10^{-3}$ kg/m/s (when held constant), and $d\rho/dz = -100kg/m^4$ (when held constant). The results are presented in Figure 3-6. In both cases the variations in the volume flux are within 0.2% of the analytic result (eq. 3.1), an error that is on the same order as the noise that exists in the velocity field. Overall, these results reveal that the density gradient and the viscosity do not impact the volume flux.

The influence of the gap thickness on the volume flux is studied next. Since the maximum number of mesh points is used for all simulations, increasing the size of the system decreases the mesh density, reducing the accuracy of the measurement. The three tests use the parameters $\kappa = 10^{-9}$ m^2/s, width $= 0.025$ m, $\alpha = 26.5^o$, $\mu = 10^{-3}$ kg/m/s, and $\alpha = 26.5^o$ while the width is varied from $w = 0.025$ m to $w = 0.05$ and 0.1m. The results of this study are presented in Figure 3-7. While the percent variation in volume flux is larger than the viscosity and stratification tests, it is still less than 0.5%, which reveals that the gap thickness plays an insignificant role in the

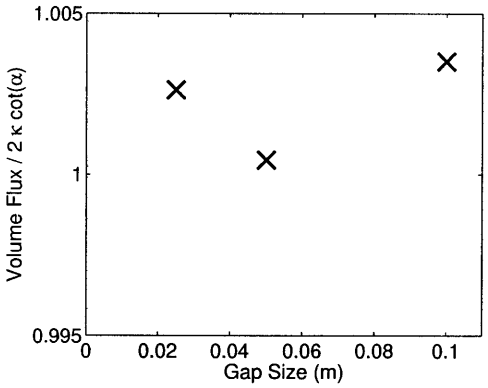

Figure 3-7: Numerical results of the influence of the chevron width on the cross-flow volume flux.

calculated result.

The first studied parameter that influences the volume flux is the slope angle of the slanted walls. This series of tests also requires the modification of the system size and mesh in all cases because as the angle grows smaller the width required for a fully developed cross flow increases. Simulations were run to ensure that the width of the domain allowed the cross-flow to develop and that the numerical results had converged. The results are presented in Figure 3-8, in which a comparison is made with the theoretical dependence $Q \propto \cot\alpha$. There is excellent agreement between numerics and theory, with most of the results falling within 0.2% of the theoretical value. For an angle of $\alpha = 7.4^o$, there is the first evidence of a departure from the theoretical result, with a discrepancy of around 0.5%. This is not surprising, however, as experimental results have previously shown that the Phillips-Wunsch analysis starts to break down around $\alpha = 5^o$ [16].

The final test is to demonstrate the linear dependence of the volume flux on the molecular diffusivity. No geometry modification is needed for this series of tests since the system shown in Figure 3-5(a) allows complete development of the cross-flow for the highest molecular diffusivity used in these studies. The parameters used for these simulations are: $\mu = 10^-3$ kg/m/s, $d\rho/dz = -100$ kg/m^4, $\alpha = 26.5^o$, and $w = .05$m. Figure 3-9 presents the results of these investigations. The results fit the linear relation very closely, all being within 0.2% of the theoretical result.

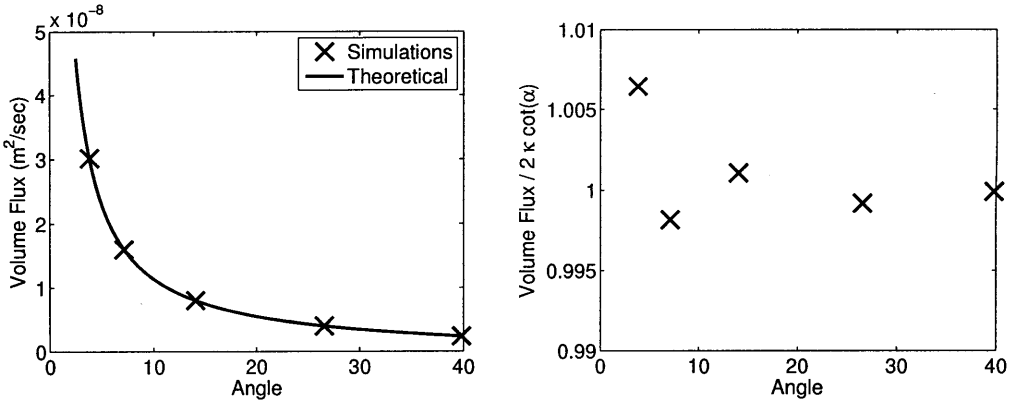

(a) (b)

Figure 3-8: (a) Plot showing the variation of the analytic and simulated volume fluxes with slope angle. (b) Value of the ratio of the simulated volume flux with the analytic flux as a function of slope angle.

In combination with the angle tests, the molecular diffusivity study indicate that measurement of the volume flux measured in a fully developed cross-flow provides an accurate means of measuring molecular diffusivity via the relation $Q = \kappa \cot\alpha$.

3.4 Experimental Demonstration

With the numerical evidence in support of a chevron system, we now demonstrate this measurement technique experimentally. This section discusses the experimental apparatus, the measurement technique, and data analysis of a proof of concept experiment.

3.4.1 Experimental Apparatus

A chevron-shaped tank is used for this experiment, based on the schematic in Figure 3-1. Using the simulations as a guide for the dimensions of the system, the acrylic tank measures a total of 30cm high, comprised of three 10cm vertical sections with the chevron section in the middle 10cm with a slope angle of 14^o. The lateral extent of the tank is 30cm to ensure that the system is nominally two-dimensional in the plane perpendicular to the induced flow. The system has a constant width of 5cm,

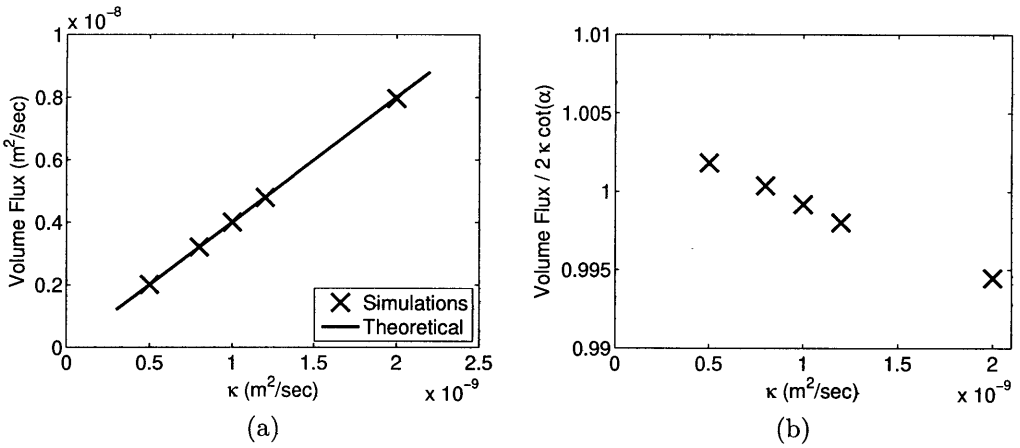

Figure 3-9: (a) Plot showing how the analytic and simulated volume fluxes vary with molecular diffusivity. (b) Value of the ratio of the simulated volume flux with the analytic flux as a function of molecular diffusivity.

which, based on the results of our simulations, is a large enough width to develop a uniform cross flow. Finally the system is filled with a linear stratification through a port at the base of the tank.

An image of the experimental arrangement is presented in Figure 3-10. The main components of the system are the tank (A), the optics board (B), the camera (C), a calibration scale (D), and a selective withdrawal needle (E). In this arrangement a laser sheet is created by a cylindrical lens mounted on the optics board, which is mounted at a 14^o angle. The laser sheet passes through the middle of the tank, so as to visualize flow in the vertical mid-plane of the center of the tank. The camera is mounted on the traverse system to the side of the tank and takes images of the flow field in the region near the tip of the chevron.

3.4.2 Experimental Procedure

To measure the molecular diffusivity of NaCl in tap-water, the chevron tank is filled with a linear stratification of strength $d\rho/dz = -500$ kg/m^4 containing the hollow glass spheres used for PIV. The filling process again utilizes the Oster double bucket method [13]. After filling is completed, the system is left to stand for four hours while transients from the filling process decay and settling of particles to their neutral

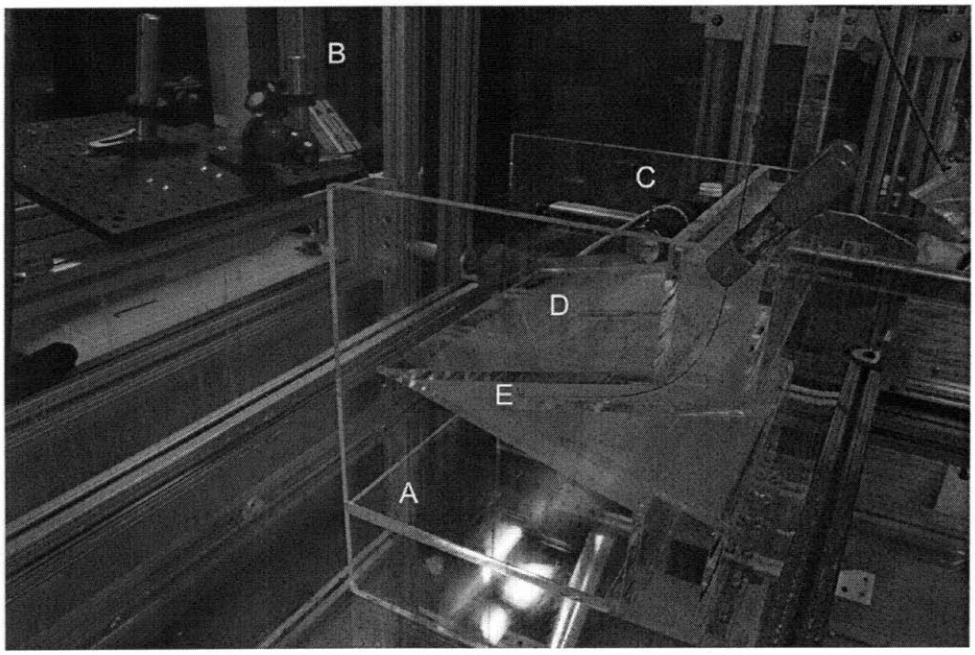

Figure 3-10: Molecular diffusivity measurement apparatus featuring (A) chevron tank, (B) optics board, (C) four megapixel camera, (D), calibration scale, and (E) selective withdrawal needle.

buoyancy heights takes place.

After transients have dissipated, the only remaining flow in the system is the convection created by diffusion-driven flows along the sloping walls. At this stage, the PIV technique is used to capture the motion of the neutrally buoyant particles suspended in the water. These particles are illuminated by the laser sheet and imaged at a rate of 0.25 Hz for sixty images. With the region of interest so close to the walls, black masking tape is placed on appropriate parts of the tank to mask the laser glare at the sloping walls. Once the data is obtained, a scale (labeled (D) in Figure 3-10) is inserted into the tank to provide a reference length scale for the PIV calculations. Finally, a needle is lowered to several depths in the tank and samples are withdrawn to measure the stratification.

This PIV analysis is performed using the same DaVis software described in Section 2.5.1. The velocity field obtained by this analysis is then studied using Matlab to determine the volume flux in the cross flow jet near the tip of the chevron. More specifically, the Matlab routine determines the vertical extent of the jet and integrates

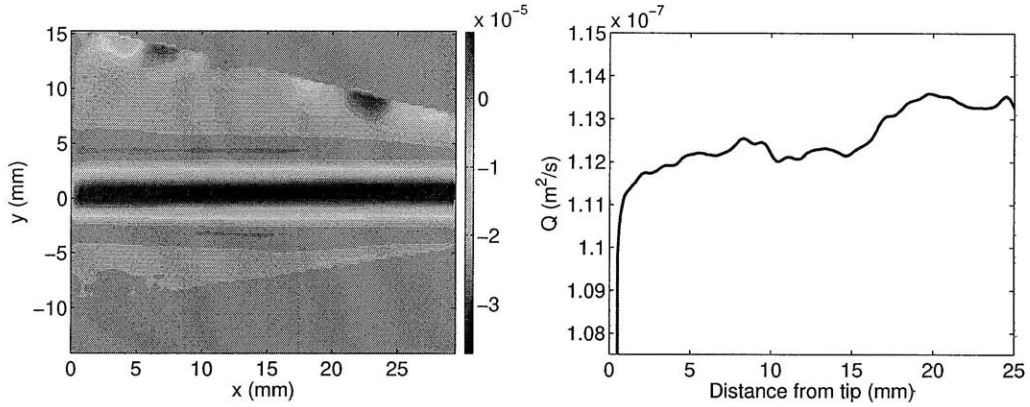

(a) (b)

Figure 3-11: (a) PIV measurement of the flow field at the tip of the chevron tank when filled with a NaCl stratification of strength $d\rho/dz = -500$ kg/m^4. (b) Volume flux measured as a function of the distance from the tip.

the horizontal velocity over this height to determine the total volume flux. This measurement is performed at multiple horizontal locations along the jet.

3.4.3 Molecular Diffusivity Measurement Results

A proof of concept experiment is performed to demonstrate that this is a feasible experiment that yields reasonable results. The PIV measurements, which present the horizontal velocity field, are presented in Figure 3-11a. The dominate feature of this measurement is the horizontal jet with peak velocity $\sim 4 \times 10^{-5}$m/s. This result matches the simulation, which also predicts a dominant jet originating at the chevron tip, and negligible flows in the rest of the bulk. It should be noted that there is still a little particle settling in this data set, and so velocity measurements in the vertical direction (not presented here) were found to contain a little noise. Also the tape, used to mask the laser glare, asymmetrically blocks out some of the velocity data.

The results of the Matlab analysis program are presented in Figure 3-11b, in which the typical volume flux is 1.13×10^{-7}m^2/s. There is a variation in the volume flux as a function of distance from the tip on the order of 1%. Using this measured volume flux and the equation

$$\kappa = \frac{Q_m}{2\cot\alpha} \tag{3.6}$$

where Q_m is the measured volume flux, the molecular diffusivity of NaCl in tap-water is found to be $1.40 \pm 0.02 \times 10^{-9}$ m^2/s. This value is approximately equal to the published value of 1.47×10^{-9} m^2/s [20]. A potential reason for the small discrepancy between these two values is that we simply used regular tap-water and a non-pure salt.

3.5 Conclusions and Future Works

This chapter demonstrates a new method for measuring molecular diffusivity by exploiting diffusion-driven flow. The chevron concept is proposed to focus the cross-flows of diffusion-driven flow in a finite fissure to facilitate easy measurement. Numerical simulations confirm that this is a viable method of measuring the molecular diffusivity of a stratified system. Finally, through the development of an experimental apparatus and procedure, it is demonstrated that this method does produce a reasonable measure of the molecular diffusivity.

The main focus of future works on this subject will be experimental. Tests using pure salts and water need to be performed to determine how results from this measurement method compare with existing and accepted results. Once the method is confirmed, it will be important to improve upon the experimental procedure to simplify the measurement process. One research avenue is to determine a way to measure the volume flux without having to use PIV. An issue with the interferometric method [1] is that it requires highly specialized equipment. PIV, however, requires a high powered laser, optical system, and a camera, so in this regard the new method is not much better. One possibility is to find a relationship between the peak velocity and the volume flux.

Chapter 4

Conclusion

The objective of this thesis is to present two novel applications of diffusion-driven flow. The first result demonstrates that it is possible to propel an object in a stratified fluid via the diffusion-driven flows that arise on its sloping surfaces. An experimental demonstration of this concept was performed and the parameter study provides an understanding of the influences of various parameters on the propulsion speed. Our studies conclude that the non-dimensional speed of the wedge is a function only of its shape (angle of inclination and aspect ratio). In order to determine a picture of the flow field around a moving wedge, particle imaging velocitimtry (PIV) is used to calculate the local velocity field in the horizontal and vertical mid-planes of the wedge. Comparison of the experimental velocity field with the results of a three-dimensional simulation provided insight into the propulsion mechanism. Finally, analysis performed on the data produced by this simulation demonstrates that there is a density perturbation in the boundary layer. This perturbation induces both a velocity and pressure field perturbations, and the propulsion mechanism, to leading order, can be attributed to this pressure perturbation. This result extends beyond diffusion-driven flows. An exciting area of research is to determine whether similar buoyancy-driven flows that develop along heated or cooled surfaces, which have a much stronger velocity field, have the potential to propel an object faster.

The other application introduced in this thesis is a new method to measure the molecular diffusivity. Using a chevron shaped system filled with a stratification,

diffusion-driven flows induce a cross-flow jet containing a volume flux that is a function only of the sloping wall angle and the molecular diffusivity. This relationship is confirmed numerically by a parameter study performed in COMSOL. With the results supporting the concept, an experimental apparatus was designed, and a proof of concept experiment executed for NaCl diffusing in tap-water yielded a result within 5% of the published value. With continued development, this novel measurement technique has the potential to become a standard method of measuring the molecular diffusivity of systems.

Bibliography

[1] E. Alanis, G. Romero, and C. Martinez. Interferometric measurement of diffusion coefficients through a scanning laser beam. *Opt. Eng.*, 39:744, 2000.

[2] V. G. Baidulov, P. V. Matyushin, and Yu. D. Chashechkin. Evolution of the diffusion-induced flow over a sphere submerged in a continuously stratified fluid. *Fluid Dynamics*, 42(2), 2007.

[3] P. G. Baines and F. Guest. The nature of upstream blocking in uniformly stratified flow. *J. Fluid Mech.*, 188:23, 1988.

[4] M. F. Barad, P. Colella, and S. G. Schladow. An adaptive cut-cell method for environmental fluid mechanics. *Int. J. Numer. Meth. Fluids.*, 60:473–514, 2009.

[5] G. K. Batchelor. *An Introduction to Fluid Dynamics.* Cambridge University Press, 1967.

[6] E. Buckingham. The principle of similitude. *Nature*, 1925.

[7] S. C. Chapra and R. P. Canale. *Numerical Methods for Engineers.* Mc Graw Hill, fifth edition, 2005.

[8] E. L. Cussler. *Diffusion: mass transfer in fluid systems.* Cambridge University Press, 2009.

[9] A. Fick. Ueber diffusion. *Poggendorff's Annalen.*, 94:59–86, 1855.

[10] R. Heitz, T. Peacock, and R. Stocker. Optimizing diffusion-driven flow in a fissure. *Physics of Fluids*, 17, 2005.

[11] E. Luna, A. Cordova, A. Medina, and F. J. Higuera. Convection in a finite tilted fracture in a rock. *Phys. Lett. A*, 300:449, 2002.

[12] J. Oerlemans and B. Grisogono. Glacier winds and parameterization of the related heat fluxes. *Tellus*, 54:440, 2002.

[13] G. Oster. Density gradients. *Sci. Am.*, 1965.

[14] M. A. Page and E. R. Johnson. On steady linear diffusion-driven flow. *J. Fluid Mech.*, 606:433, 2008.

[15] M. A. Page and E. R. Johnson. Steady nonlinear diffusion-driven flow. *J. Fluid Mech.*, 629:299, 2009.

[16] T. Peacock, R. Stocker, and J. Aristoff. An experimental investigation of the angular dependence of diffusion-driven flow. *Phys. Fluids*, 2004.

[17] O M. Phillips. On flows induced by diffusion in a stably stratified fluid. *Deep-Sea Res.*, 17:435–443, 1970.

[18] L. Prandtl. *The Essentials of Fluid Dynamics.* Blackie, 1952.

[19] M Raffel, C. E. Willert, S. T. Wereley, and J. Kompenhans. *Particle Image Velocimetry: A Practical Guide.* Springer, second edition, 1998.

[20] J. A. Rard and D. G. Miller. The mutual diffusion coefficients of nacl-h_2o and $cacl_2$-h_2o at 25°c from rayleigh interferometry. *Journal of Solution Chemistry*, 8(10), 1979.

[21] R. W. Schmitt. Double diffusion in oceanography. *Annu. Rev. Fluid Mech.*, 26:255, 1994.

[22] J. Siepmann and N. A. Peppas. Modeling of drug release from delivery systems based on hydroxypropyl methylcellulose (hpmc). *Advanced Drug Delivery Reviews*, 48:139, 2001.

[23] R. H. Stokes. An improved diaphragm-cell for diffusion studies, and some tests of the metod. *J. Am. Chem. Soc.*, 72:763, 1950.

[24] C.R. Torres. Personal communications, 2010.

[25] Tropea, Yarin, and Foss. *Springer Handbook of Experimental Fluid Mechanics.* Springer, 2007.

[26] F. M. White. *Fluid Mechanics.* Mc Graw Hill, fifth edition, 2003.

[27] A. W. Woods. Boundary-driven mixing. *J. Fluid Mech.*, 226:625, 1991.

[28] A. W. Woods and S. J. Linz. Natural convection in a tilted fracture. *J. Fluid Mech.*, 241:59, 1992.

[29] C. Wunsch. On oceanic boundary mixing. *Deep-Sea Res.*, 17:293–301, 1970.